Biophysical Journal
Article

Biophysical Society

Nucleation causes an actin network to fragment into multiple high-density domains

Aravind Chandrasekaran,[1,3] Edward Giniger,[3] and Garegin A. Papoian[1,2,*]
[1]Department of Chemistry and Biochemistry, University of Maryland, College Park, Maryland; [2]Institute for Physical Science and Technology, University of Maryland, College Park, Maryland; and [3]National Institutes of Neurological Diseases and Stroke, National Institutes of Health, Bethesda, Maryland

ABSTRACT Actin networks rely on nucleation mechanisms to generate new filaments because spontaneous nucleation is kinetically disfavored. Branching nucleation of actin filaments by actin-related protein (Arp2/3), in particular, is critical for actin self-organization. In this study, we use the simulation platform for active matter MEDYAN to generate 2000 s long stochastic trajectories of actin networks, under varying Arp2/3 concentrations, in reaction volumes of biologically meaningful size ($>$20 μm^3). We find that the dynamics of Arp2/3 increase the abundance of short filaments and increases network treadmilling rate. By analyzing the density fields of F-actin, we find that at low Arp2/3 concentrations, F-actin is organized into a single connected and contractile domain, while at elevated Arp2/3 levels (10 nM and above), such high-density actin domains fragment into smaller domains spanning a wide range of volumes. These fragmented domains are extremely dynamic, continuously merging and splitting, owing to the high treadmilling rate of the underlying actin network. Treating the domain dynamics as a drift-diffusion process, we find that the fragmented state is stochastically favored, and the network state slowly drifts toward the fragmented state with considerable diffusion (variability) in the number of domains. We suggest that tuning the Arp2/3 concentration enables cells to transition from a globally coherent cytoskeleton, whose response involves the entire cytoplasmic network, to a fragmented cytoskeleton, where domains can respond independently to locally varying signals.

SIGNIFICANCE Dendritic actin networks are essential to generate protrusive forces in cells. However, the micron-level spatial organization that results from nanometer-level Arp2/3 dynamics is still poorly understood. To address this, we use a computational model, MEDYAN, to study the spatial organization of actin at various Arp2/3 concentrations and discover that elevated Arp2/3 levels favor formation of short filaments ($<$1 μm). Consequently, while at low Arp2/3 concentrations, actin filaments come together processively to form a globally contractile network, at high Arp2/3 concentrations, multiple, spatially separated actin networks form, leading to network fragmentation. We propose that such disconnected network states could enable cells to sustain spatially heterogeneous chemical fluxes and force transmission, facilitating spatially tuned responses to a wide range of signaling cues.

INTRODUCTION

Biological systems rely on specific patterns of self-organization to produce cell shapes and distributions of cellular constituents that perform physiological functions effectively. The structural properties of cells are controlled by the cytoskeleton, which is a network of filamentous proteins such as actin, microtubules, and intermediate filaments. Actin, the most abundant cytoskeletal protein, enables critical biological processes through assembly and disassembly of filaments, motor proteins (myosin) that walk along filaments to exert forces, and passive crosslinkers that tune the connectivity of the network (1,2). These molecules self-assemble under the guidance of precisely controlled signaling pathways to form micron-scale structures that give structural stability and dynamic adaptability to cells. As the collective behavior of the multi-component actin network *in vivo* is exceptionally complex, *in vitro* studies using minimal sets of reconstituted components have been essential to reveal the detailed biophysical mechanisms that underly actin organization. A great challenge, however, is to understand how these simple components come together to produce the diversity of large-scale structures observed in cells.

Submitted November 18, 2021, and accepted for publication July 28, 2022.
*Correspondence: gpapoian@umd.edu
Editor: Timo Betz.
https://doi.org/10.1016/j.bpj.2022.07.035

The cytoskeleton is extremely versatile in that its components can form a wide array of structures that are optimized for specific needs. For example, in eukaryotic cells that lack a cell wall, actin forms a pseudo-planar network of filaments right under the plasma membrane to form the actin cortex. Together with myosins and other actin-binding proteins, the cortex offers mechanical stability to the cell. The actin organization and dynamics in this architecture have been studied extensively (3–5). Another, very different, actin-dependent structure is found in the axonal growth cones of neurons. The growth cone is the highly branched, filamentous structure at the tip of a growing axon that produces protrusive forces to promote extension of the axon and steer its growth through the extracellular medium to reach specific neuronal targets. Extensive experimental studies have identified many cytoskeletal components involved in growth cone motility. However, it has been challenging to link the nano-scale chemical processes these molecules control with the micron-scale network organization they produce in the growing axon.

Genetic and cell biological experiments suggest that the branched actin nucleating factor, actin-related protein 2/3 (Arp2/3), and myosin are particularly important for growth cone function. As spontaneous nucleation of actin filaments is kinetically disfavored, cells rely on nucleating factors such as Arp2/3, formin, spire, and liemodulin to generate new filaments (6). Thus, cells dynamically assemble actin networks by tightly controlled spatial localization and activation of such nucleation factors. Among the various nucleating factors, branched actin nucleation has been implicated in maintaining a coherent growth cone and is highly regulated as a downstream effector in key signaling pathways (7,8). Branched nucleation proceeds by nucleating new offspring filaments on the side of preexisting parent filaments at an angle of approximately 70° (9,10), primarily by the Arp2/3 complex, which accelerates nucleation by mimicking the presence of two actin monomers (11). Branching and debranching activities have profound effects on cell shape and dynamics (12,13) and indeed are commonly found to be central targets of the external signals that regulate cytoskeletal events (8,14–16). This mechanosensitive process is necessary to generate forces against the plasma membrane to drive motility (17). Moreover, as the elongation capacity of an actin network is limited by the number of filaments, mechanisms such as actin nucleation and severing lead, respectively, to a surge in extensible filaments and, in the abundance of the polymerizable actin pool, resulting in a dynamic actin network with augmented turnover. Hence, it is essential to understand the effects of Arp2/3 in determining actin network architecture, which, in turn, gives rise to its salient mechanical properties.

In conjunction with actin architecture, forming stable and dynamic cytoskeletal structures also requires a delicate balance between motor-driven forces and viscoelastic dissipation (18–21). Thus, large-scale remodeling of networks through contractile forces and actin turnover is crucial for effective force production that leads to locomotion and growth. Studies of actin networks, and their interaction with crosslinkers and myosins, have uncovered fundamental organizational principles of linear and planar actin structures (2,4,22–25). However, just as the crosstalk between contractility and actin turnover has proven to be essential for dissecting cortical tension (26), to understand the mechanics of the growth cone cytoskeleton, it is essential to study a minimal growth cone mimic with actin, crosslinkers, myosins, and constitutively active Arp2/3 to dissect the crosstalk between actin turnover and myosin contractility.

While computational studies on actin networks have helped identify kinetic (27) and mechanical (28) differences between linear and dendritic actin networks, computational limitations have prevented understanding network organization in the large-scale dendritic networks that form *in vivo*. Therefore, inspired by the actin organization observed from *in vivo* imaging of a growth cone in the developing *Drosophila* wing (called TSM1 (29,30)), we set out to computationally prepare actin filaments, crosslinked by α-actinin and myosin, and subject them to varying concentrations of the branching nucleator Arp2/3 in a cylindrical volume whose dimensions approximate that of an *in vivo* TSM1 growth cone. We reasoned that investigation of the properties of such a network at larger, multi-micron-length scales might reveal emergent properties that are not readily apparent from order parameters estimated at sub-micron length scales (such as nematic order parameter, contact number, coordination number, and radial distribution function). Hence, we chose to employ spatial density field analysis (pixel intensity analog) to understand spatial and temporal patterns in the micron-level network organization of disordered actin networks.

Here, we demonstrate that Arp2/3-driven nucleation drastically alters network organization in a concentration-dependent manner between a connected, globally contractile state versus a more fragmented association of distinguishable domains that are only relatively weakly linked to one another. We show that the global actin network is characterized by actin-rich local domains of heterogeneous volume that dynamically exchange filamentous actin with one another and with the actin-depleted surrounding. We further find that conditions with reduced Arp2/3 tend toward a smaller number of larger domains, while higher levels of Arp2/3 fragment the network into larger numbers of smaller domains. We further establish that the mechanism by which nucleation activity controls the size and number of high-density domains is mediated through modulating the distribution of actin filament lengths, which acts cooperatively with myosin contractility to regulate the organization of the overall actomyosin network at the multi-micron scale. Thus, at low Arp2/3 concentrations, where long actin filaments are abundant, myosin-driven forces favor globally contractile networks. In contrast, the predominance of short filaments at high Arp2/3 concentrations limits long-range, myosin-dependent interactions, favoring

condensation of actin into a multiplicity of small, locally contractile domains. Treating the time evolution of the number of actin domains as a stochastic process with state-dependent drift and diffusion, we show that the fragmented state evolves stochastically due to the delicate balance between domain-split and domain-merge events. Finally, we discuss the biological significance of toggling actin network organization between globally connected versus relatively fragmented states.

MATERIALS AND METHODS

All simulations performed in this work were carried out using MEDYAN (31), a mechano-chemical force field, to simulate active networks. MEDYAN encodes an explicit filament model that is coupled with a diffusive phase of reactive molecules. The transport dynamics of the diffusive phase and its chemical interactions with the filament phase are evolved using an efficient version of the Gillespie algorithm called the next reaction method (32). MEDYAN's stochastic reaction-diffusion framework also accounts for the force-sensitive changes to the reaction rates. This comprehensive modeling strategy has been instrumental in understanding thermodynamic principles of self-organization of actin networks (18) and mechanistic details that aid formation and contractility in specific actin structures, including bundles (33,34), rings (35), and isotropic networks (31,36).

Inspired by axonal growth cones (29,30) and microvilli (37) observed *in vivo*, we chose to simulate actin networks in a cylindrical reaction volume of 2-μm diameter and 7.5-μm height to avoid artificial edge-dependent biases found in cuboidal systems and to allow for emergent effects of larger absolute physical scale (31). Simulations contained 20-μM diffusing G-actin and were initialized with 400 randomly located and randomly oriented F-actin seed filaments, each 40-monomers long (108 nm). These seed filaments represent ~5.3% of the total actin initially present in the volume and allow the simulations to bypass an otherwise lengthy lag period for initial actin nucleation. We note, however, that the actin monomers contained in these seeds are turned over by treadmilling within the first 300 s of the simulations. In MEDYAN, filaments are represented as rigid cylinders that are joined at hinge points. The latter helps us define bending deformations, tuned to reproduce F-actin's persistence length (38). While longitudinal stretching and compression are also modeled, they are small in amplitude because of very high stiffness of actin polymers (31,39). Each cylindrical element is 40 (actin) monomers long, exposing four binding sites for binding linkers, motors, or brancher molecules.

Stochastic chemical evolution in MEDYAN is achieved through the next reaction method (32). Diffusion and reaction events are modeled at single-molecule resolution. Structural description of filaments along with necessary mechanical forcefields describe stress build-up during chemical evolution (31). The network is mechanically equilibrated every 25 ms of chemical evolution using a gradient descent algorithm, accounting for mechano-chemical effects and feedbacks. In MEDYAN, unbinding of α-actinin and myosin minifilaments are mechano-sensitive, modeled as slip and catch bonds, respectively. Unbinding rates are calculated at the end of every minimization cycle based on corresponding instantaneous forces. Chemical evolution and mechanical equilibration steps are iterated to generate 2000-s-long trajectories. Please refer to the supporting methods for a detailed description of key features of MEDYAN, along with the chemical reactions considered in this study.

In order to create conditions for the formation of a contractile network, we introduced non-muscle myosin IIA minifilaments (mole ratio of myosin heads to actin = 0.1) and α-actinin (mole ratio of α-actinin to actin = 0.01). Linear networks described above were evolved for 1 s before activating Arp2/3 molecules. In cells, Arp2/3 activation is restricted to membranes, which are rich in Arp2/3 activators such as WASP, WAVE, and N-WASP. In axons and growth cones, experimental images have revealed a dense concentration of internal membranes, including membrane-bound organelles such as endoplasmic reticulum and cytoplasmic transport vesicles, among others, which presumably can serve this function (29,40). We, therefore assume that constitutively active Arp2/3 is readily available throughout the growth cone cytoplasm since explicit consideration of Arp2/3 association with such complex membrane surfaces would be computationally expensive and would require extensive assumptions about the internal organization of the growth cone cytoplasm. Thus, we model bulk nucleation of actin filaments mediated by Arp2/3 binding.

In our model, Arp2/3 binding produces an offspring along the side of the mother filament at a 70° angle, forming a nascent dendrite (9,41). The offspring filament's minus end is protected from (de)polymerization events in the Arp2/3-bound state. Conversely, Arp2/3 unbinding results in a free offspring filament, a diffusing Arp2/3 molecule, and a free binding site on the parent filament. We model Arp2/3 unbinding as a force-sensitive slip bond with a characteristic unbinding force of 6pN([42]). All simulation parameters and the number of replicates generated in this study are elaborated on in Table S1.

Note that the simulations analyzed in detail here are a sub-set of the simulations used to model actin architecture in a developing axon *in vivo* in a parallel publication from our group (43). The results of the two papers, while consistent, are entirely independent; no analysis is repeated in both manuscripts.

RESULTS

Increased Arp2/3 activity reduces the dispersity of filament lengths and increases network treadmilling rate

To understand the impact Arp2/3 branching has at the filament level, we simulated actin networks at Arp2/3 concentrations 0, 1, 5, 10, 25, and 50 nM (six replicates per concentration). To ensure that our simulations have reached steady state, we looked at structural and chemical properties of the network (filament length distribution [Fig. 1 *a*], network treadmilling rate [Fig. 1 *b*, explained below], and radius of gyration [Fig. S2]). The low variability of these parameters both between trajectories and in the last 500 s of our trajectories confirmed that the actin network has attained a steady state. As expected, in linear networks ([Arp2/3] = 0 nM), the seed filaments extended into long filaments by consuming the diffusing pool of G-actin. With the addition of Arp2/3, filament distribution bifurcates into a population of short filaments nucleated by Arp2/3 and a population of extended seed filaments (Figs. 1 and S1; supporting material). A further increase in Arp2/3 concentration results in networks dominated by dendritic nucleation and characterized by extremely short filaments (<0.5 μm). Thus, increasing Arp2/3 activity increases the filament nucleation rate, resulting in a steady state characterized by short filaments.

We wondered whether actin treadmilling could account for the effect of Arp2/3 on filament length. We therefore investigated how the treadmilling rate of the network depends on the Arp2/3 concentration. Treadmilling is a steady-state behavior where filaments have stable average lengths as the retraction rate of minus ends matches the extension rate of plus ends. Hence, we define treadmilling rate as the average of the number of monomers that have depolymerized from the minus end and the number of monomers that have polymerized onto the

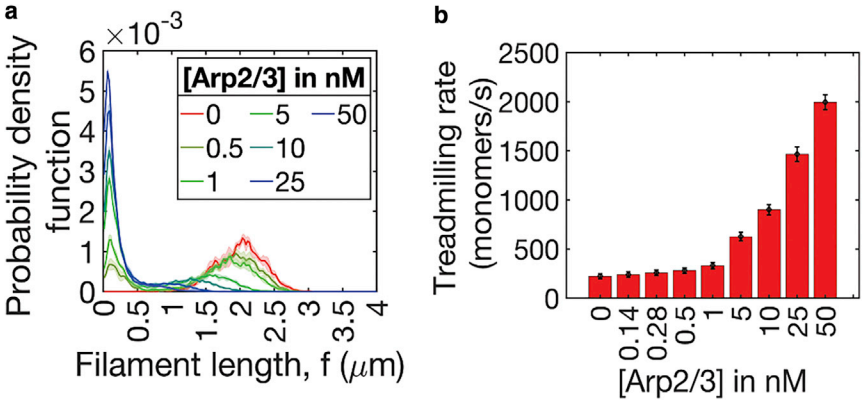

FIGURE 1 Dendritic activity in networks causes a reduction in filament length and increases monomer replacement by treadmilling. (*a* and *b*) The plot of (*a*) filament length and (*b*) network treadmilling rate of networks at various Arp2/3 concentrations. (*a*) Solid lines and shaded areas represent the mean and standard deviation, respectively, of filament lengths from six replicates. (*b*) Mean treadmilling rate of the network is plotted as a bar graph, with error bars representing standard deviation. Networks' approach to steady state was quantified based on time invariance of mean treadmilling rate. As the treadmilling rate stabilized around 1500 s, data from the last 500 s of trajectories (six replicates, sampling frequency = 5 s) was employed in (*a*) and (*b*). To see this figure in color, go online.

plus end in 1 s (27). We find that the treadmilling rate (Fig. 1 *b*) at steady state increases with Arp2/3 concentration due to the increase in the number of filament ends from Arp2/3-based nucleation. (27) Additionally, Arp2/3 unbinding exposes the minus end to fluctuations from filament polymerization and depolymerization reactions. We therefore speculate that the combination of finite-bound lifetimes for the Arp2/3-parent-offspring filament complex ($\tau = 50$ s) (42) and mechano-sensitive offspring unbinding that are incorporated in our model (based on experimental observations (44)) contribute further to the enhanced treadmilling rate. Varying Arp2/3-unbinding rates at [Arp2/3] = 25 nM, we find that slower unbinding leads to increased abundance of longer filaments, reduced number of filaments, and diminished treadmilling rates (supporting material; Fig. S3). Taken together, the results shown in Fig. 1 suggest that under the influence of Arp2/3, branching activity produces a population of short filaments and that the networks experience enhanced treadmilling rate.

Arp2/3 alters the hierarchical organization of actin networks

Having seen how Arp2/3 affects the properties of actin filaments, we then investigated the influence of Arp2/3 on the network-level organization of actin. To achieve this, we mapped the high-resolution actin filament coordinates onto a coarse-grained density field. Dividing the reaction volume into voxels of size (x, y, z = 100, 100, 100 nm), we counted the number of F-actin monomers enclosed in each voxel to define local actin density through mean filtering. The mean-filtering technique is helpful to prevent large voxel-to-voxel variation in local densities that might arise from mapping fine filament structure to coarse density field (45,46).

To understand how actin is organized in the reaction volume, we visualize the density field at various voxel concentration thresholds (Fig. 2 *a*). This visualization is similar to observing fluorescently labeled experimental actin networks at varying intensity thresholds. When all voxels with F-actin are considered (threshold of 0 μM), we see minor differences from changing the Arp2/3 concentration; there is actin present throughout the reaction volume. Density fields at higher thresholds, however, reveal drastic differences in actin organization. When the threshold is set to the bulk actin concentration of our simulations (20 μM) (Fig. 2 *a*), we see that actin is not distributed uniformly throughout the volume but rather is concentrated in spatially distinguishable clusters of voxels, here termed domains, whose size and number vary over the Arp2/3 concentrations studied.

Examining actin organization at the 40-μM threshold, we see stark differences depending on branching activity. At low Arp2/3 concentrations, F-actin contracts globally into a single domain. Increasing Arp2/3 concentration to 10 nM results in a network that is composed of two high-density actin domains. At higher Arp2/3 concentrations ([Arp2/3] = 25 nM and [Arp2/3] = 50 nM), the number of domains increases, suggesting that the actin distribution is spatially heterogeneous. Increasing thresholds to 5× bulk actin concentration (100 μM) does not reveal significant changes in trends observed compared with the 40-μM threshold.

To characterize further the trends in network organization observed above, we quantified the number of distinguishable domains as we varied the threshold actin concentration. Using a breadth-first search algorithm, we identified domains formed of voxels where actin concentration is greater than a threshold and with a minimum volume (27 voxels, corresponding to ~0.03 μm^3) and termed them high-density actin domains. The choice of minimum volume threshold does not affect the qualitative trends observed (Fig. S4.) Figs. 2 *b* and *c* elucidate the nature of actin organization over a wide range of threshold concentrations. We see that the trends in the number of domains from changing Arp2/3 levels do not change when the actin density field is visualized at 2–10× bulk actin concentration (40–200 μM). We also find that under all Arp2/3 concentrations studied, most of the actin (>80%) is found in regions where the local voxel density is 20 μM and above (Fig. 2 *c*). Thus, actin's overall hierarchical organization is dictated by a combination of filament length and, as we will show below, myosin activity. To quantify further the trends

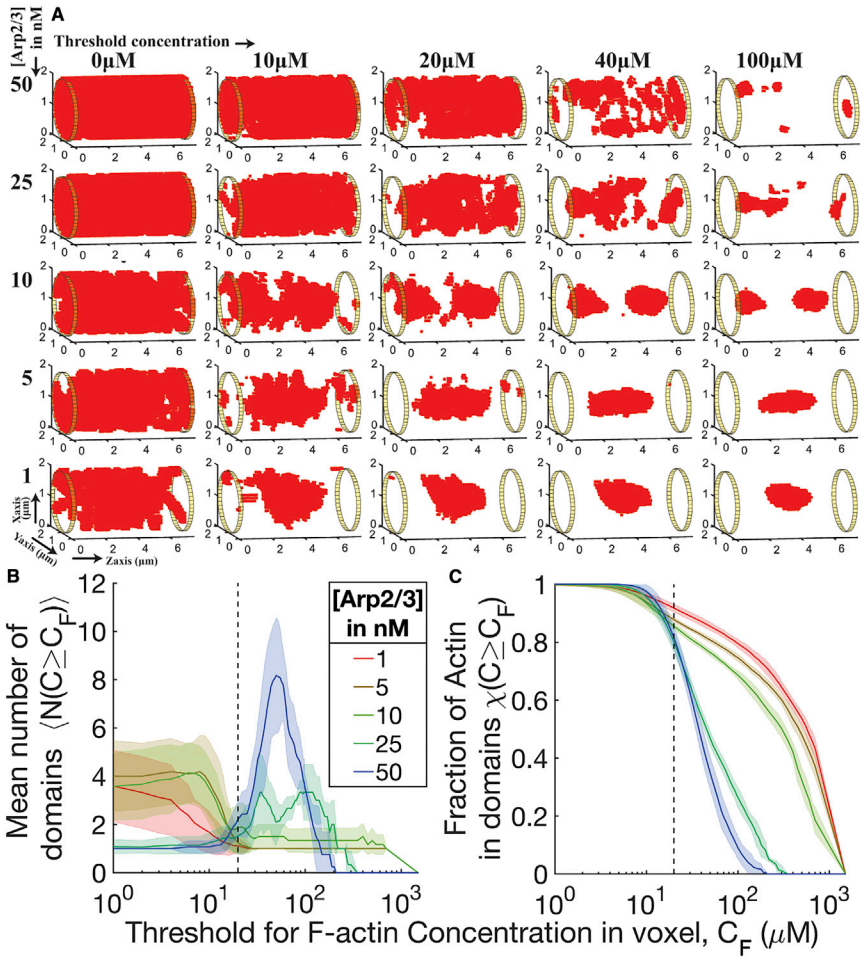

FIGURE 2 Visualization of actin density field reveals Arp2/3-driven changes to actin organization. (*a*) We visualize representative final snapshots from our simulations at various Arp2/3 concentrations as a density field. Cylindrical reaction volume is discretized into voxels of size (100, 100, 100) nm to define local F-actin density. The ends of cylindrical volume are shown as 50-nm-thick yellow cylinders. Please refer to the materials and methods for more information on the actin density field computation. Red squares represent the center of mass of voxels that contain actin above the threshold concentrations (listed above). (*b*) Plot of the number of domains identified when viewing the actin density field at various threshold concentrations from last 100 s of snapshots (sampling frequency = 5 s) of six replicates. Solid line represents mean, and shaded area represents standard deviation. The *X* axis is shown on a logarithmic scale, and the bulk actin concentration is shown as a dotted line. Note that the apparent fine structure of fluctuations observed in 25- and 50-nM profiles between 40- and 200-μM thresholds correspond to small (1–2 unit) fluctuations in the number of domains identified. (*c*) The fraction of total actin monomers included in identified domains was found by integrating over the density field and is plotted versus threshold actin concentrations. The dotted line represents bulk actin concentration (20 μM). Solid lines represent mean, and shaded area represents standard deviation. The fraction of total actin included in the domains reduces with increasing [Arp2/3]. To see this figure in color, go online.

in network organization observed above, we investigated the actin density fields at a threshold concentration of 40 μM, twice the bulk actin concentration in the network. This threshold was selected to provide maximum sensitivity for identifying the number of domains at various [Arp2/3] while ensuring that the domains contain the majority of total actin in the network. Please refer to the supporting results (Fig. S9) for a discussion on the role of threshold concentration. The distribution of domain volume from the last 100 s (sampling frequency = 5 s) of trajectories under a threshold concentration of 40 μM revealed remarkable differences in domain organization (Fig. 3). As Arp2/3 concentration is increased, two trends are observed. First, median domain size decreases. Second, heterogeneity of domain size initially increases, peaking at intermediate concentrations of Arp2/3, before beginning to reduce again at the highest concentrations. We postulate that heterogeneity arises from the stochastic fluctuation of a balanced set of competing factors that drive domain expansion and contraction, respectively, but which resolve in favor of domain condensation versus fragmentation at the two extremes of Arp2/3 level. The results discussed above suggest that Arp2/3 alters the organization of the F-actin network, effectively causing fragmentation into domains with heterogeneous size distributions. This conjecture will be examined in more detail below and in the discussion.

Increased Arp2/3 activity results in multiple, fragmented high-density domains in actin network

To understand the mechanism by which networks at higher Arp2/3 concentrations fragment into multiple domains, we investigated the time profile of the actin density field at a concentration threshold of 40 μM. Fig. 4 shows representative time-dependent snapshots at various Arp2/3 concentrations. We see that, initially, networks at all Arp2/3 concentrations are composed of spatially fragmented domains. As the simulation proceeds, we find that spatial segregation of the network into actin-rich and actin-depleted regions occurs in an Arp2/3-concentration-dependent manner. In networks with <10 nM Arp2/3 concentrations, the domains merge with time, resulting in a single, connected domain. At Arp2/3 concentrations of 10 nM and above, actin networks initially contract and merge through agglomeration of preexisting domains. However, at later stages in the simulation, these high-density actin domains separate from one another, resulting in a network

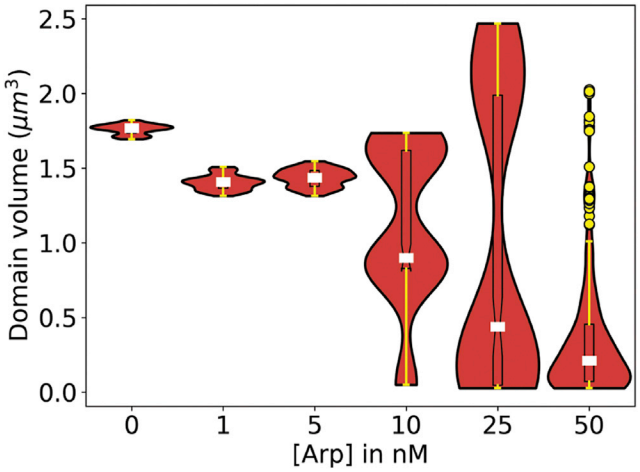

FIGURE 3 Distribution of high-density actin domain volume reveals differences in actin organization resulting from Arp2/3 activity. Volume distributions of high-density actin domains identified at 40-μM threshold at various Arp2/3 concentrations from the last 100 s of the trajectories (six replicates, sampling frequency = 5 s) are represented as violin plots. The boxplot shows the 25th–75th percentile represented as a box with the median shown as white lines. Whiskers are shown as solid yellow lines, with outlier data points represented as yellow circles. Data shown are collected from last 100 s of all six replicates per [Arp2/3]. To see this figure in color, go online.

where high-actin-concentration regions are again spatially fragmented. Together, these results demonstrate that the mechanism of actin organization changes depending on Arp2/3 concentration.

To gain more insights into the Arp2/3-driven fragmentation of high-density domains, we calculated the number of distinguishable domains found in the density field at snapshots taken every 5 s (Fig. 5 *a*) using a breadth-first search algorithm over the voxels that satisfy the concentration threshold. Looking at the fraction of total F-actin that is contained in high-density domains (Fig. 5 *c*), we first see a sharp increase until 500 s. This is consistent with the idea that myosin activity throughout the volume first stochastically condenses the actin into local clumps whose actin concentration is above that of the bulk background (as seen in Fig. 4, *columns 1–3*), and these, in turn, coalesce into larger units. After this initial collection of actin into domains of enhanced density, the rate of F-actin accumulation slows down or even reverses slightly, dependent on the Arp2/3 level. At low Arp2/3 concentrations ($\leq$5 nM), the initial aggregation of actin is accompanied by a steady decrease in the number of domains until the entire network is composed of a single, connected domain that remains connected for the rest of the simulation. In this condition, the absolute actin concentration within the domains continues to show a steady increase with time (Fig. 5 *b*). In contrast, at higher Arp2/3 concentrations, networks evolve with a biphasic domain count profile where, during the initial phase (until 200 s), we again see a reduction in the number of high-density actin domains, but it is followed by a maturation phase where the number of domains increases. In this condition, however, increasing Arp2/3 concentration progressively limits the final actin concentration in domains (Fig. 5 *b*).

Cooperation between myosin and Arp2/3 dynamics modulates actin organization

The pattern of Arp-dependent changes to actin concentration in high-density actin domains led us to wonder if there was crosstalk between nucleation-driven treadmilling and myosin-driven contractility. To understand the role of myosin in the mechanism of Arp2/3-driven fragmentation, we studied actin networks by reducing myosin concentrations to 50% and 10% of the myosin concentration employed in simulations discussed so far and generated five replicates per [Arp2/3] myosin mole ratio pair. The number of domains from the last 100 s of the 2000-s trajectories is plotted in Fig. 6 *a–c*, and the time profiles are shown in Fig. S5. At all myosin concentrations studied, increasing Arp2/3 results in a fragmented network characterized by an elevated number of high-density actin domains. We also looked at actin concentration in the high-density actin domains to understand myosin's impact in organizing filamentous actin (Fig. 6 *d–f*). Consistent with Fig. 5 *b*, increasing Arp2/3 reduces F-actin concentration in domains. Additionally, we find that at any given Arp2/3 concentration, reducing myosin decreases actin concentration in domains consistent with the reduced contractility of the

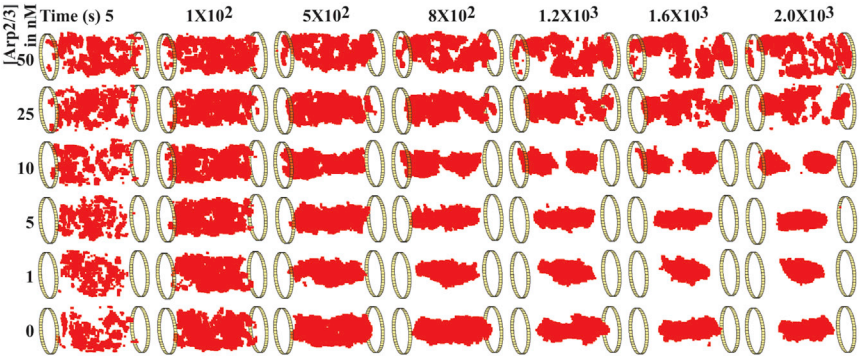

FIGURE 4 Time profiles of actin density field reveal altered network organization leading to actin fragmentation at elevated Arp2/3 concentrations. At various time points in our simulations with different Arp2/3 concentrations, representative snapshots are converted into actin density fields to reveal actin organization. The actin density field is visualized at a 40-μM threshold concentration in each case. The voxels that have a local actin concentration higher than the threshold concentration are shown in red. Timestamp in seconds is shown to the top, while Arp2/3 concentrations are mentioned on the left. Data shown here are from the final snapshot of a single replicate corresponding to each [Arp2/3]. To see this figure in color, go online.

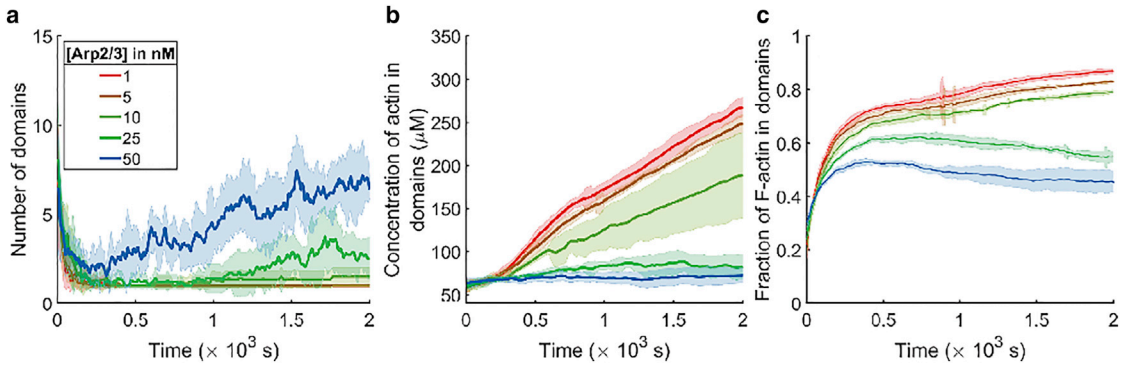

FIGURE 5 Analysis of high-density actin domains reveals Arp2/3 dependent differences in network organization. (*a*) Number of actin domains found from actin density field analyses is plotted as a time profile at various Arp2/3 concentrations. (*b*) Time profiles of actin concentration in the domains are plotted at various Arp2/3 concentrations. (*a* and *b*) Solid lines and shaded areas represent mean and standard deviation, respectively. (*c*) Time profiles of the fraction of total actin in the domains at various Arp2/3 concentrations. The solid line and shaded area represent mean and standard deviation, respectively. (*a–c*) Data shown are calculated from six replicates per Arp2/3 concentration, and data sampling frequency = 5 s. To see this figure in color, go online.

networks. The actin concentration in these domains (Fig. 6 *d–f*) reduces with increasing Arp2/3, particularly at high concentrations of myosin, but has a diminished effect as myosin level decreases, suggesting that Arp2/3 reduces actin density primarily by hindering myosin-driven contractility. We also find that the heterogeneity of these measurements within a condition tends to be maximal in parameter ranges where opposing, stochastic processes are roughly balanced, much as we found for the domain volume measurement in Fig. 3 (above).

We then asked if reducing myosin levels increases fragmentation of the actin network. Decreasing myosin to 50% and 10% causes significantly increased fragmentation of actin networks up to [Arp2/3] = 10 nM (Fig. 6 *a–c*; Wilcoxon test; all p values are listed in Table S2). At higher Arp2/3 concentrations, we find that reducing myosin to 50% does significantly increase fragmentation, but a further reduction to 10% does not affect the network fragmentation from that observed at 50% reduction (p range = 0.86–1.00). It is interesting to note, however, that under all conditions studied, reducing myosin did increase fragmentation in the initial phase (<500 s) of the trajectories (Fig. S5). This is suggestive of timescale differences in the dominant mechanism that drives actin organization in dendritic networks, perhaps accounting for the biphasic temporal evolution of domain number under conditions of high Arp2/3 (Fig. 5 *a*).

The activity of Arp2/3 alters dynamics of high-density actin domains toward fragmented states

The results above show how overall network properties evolve over time, with Arp2/3 causing global spreading and myosin producing local condensation. But how does this combination give rise to the final fragmented states that we observe? To

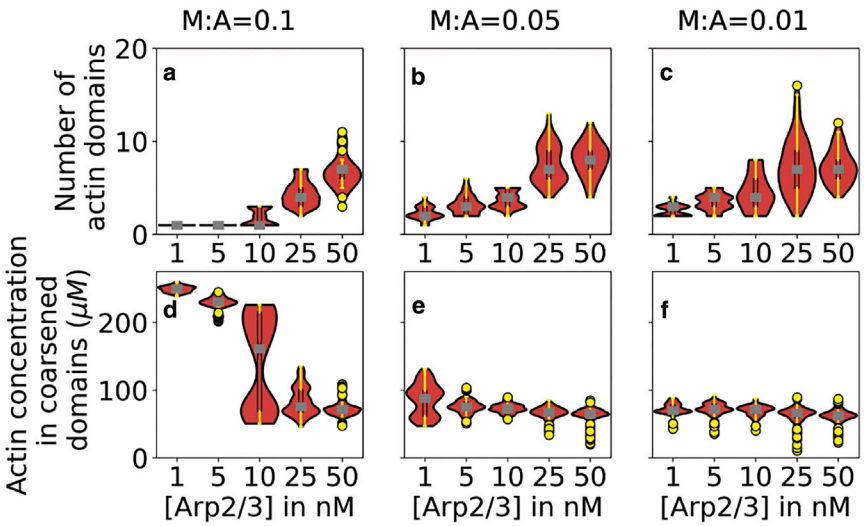

FIGURE 6 Cooperation between myosin and actin leads to network fragmentation. (*a–c*) Violin plots showing the number of domains in the actin density field obtained at a threshold concentration of 40 μM at different Arp2/3 concentrations (*X* axis). Myosin mole ratios are mentioned above each panel. (*d–f*) Violin plots showing actin concentration in high-density actin domains. Note that the domains are determined based on the mean concentration threshold, while the concentration plotted here is calculated based on actin concentration determined from filament data. Hence, the actin concentration in domains can be below the mean concentration threshold. (*a–f*) Plots also show median values (gray) and 25% and 75% quantiles as boxplots (black). Whiskers represent data ranges (yellow lines), and outlier data are plotted as yellow circles (mole ratio of myosin heads to actin = 0.1, Nsimulations = 6, mole ratio of myosin heads to actin = 0.05 and 0.01, Nsimulations = 5, data points = last 100 s, sampling frequency = 5 s). To see this figure in color, go online.

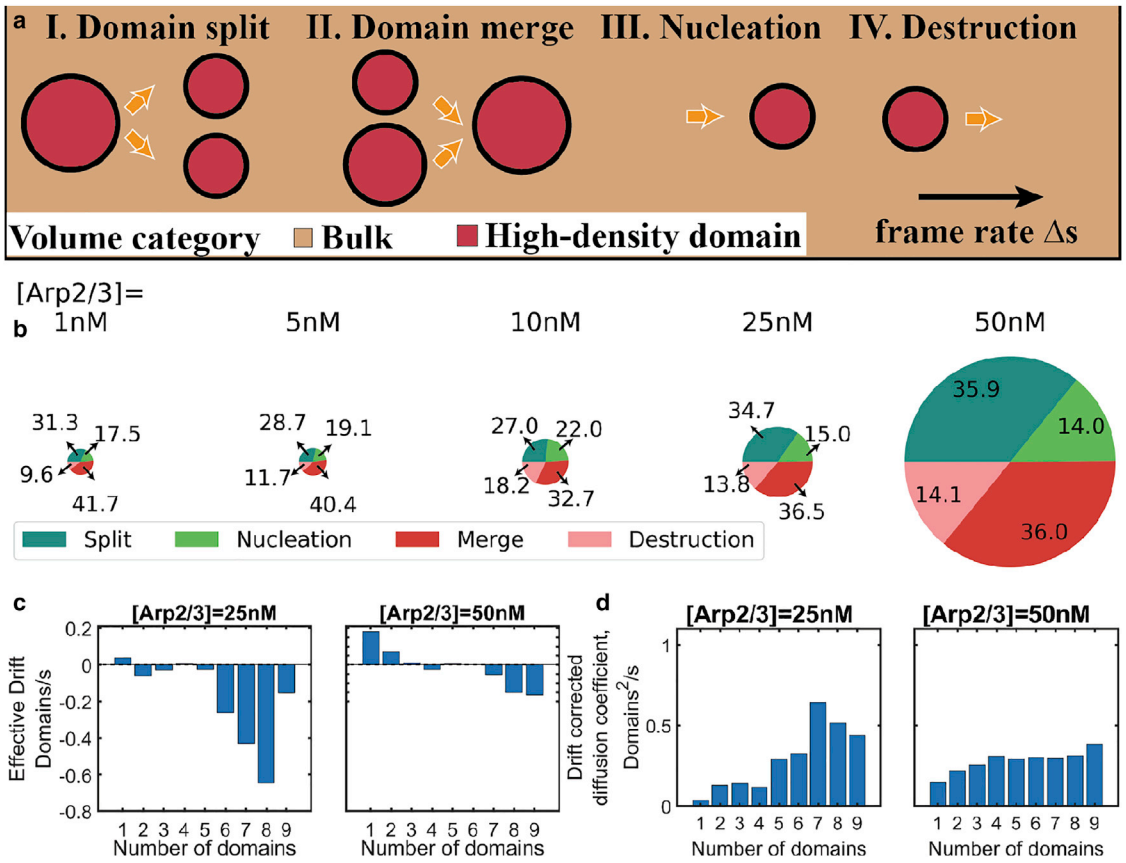

FIGURE 7 Analysis of domain dynamics reveals the underlying mechanism of F-actin organization into high-density actin domains. (*a*) The cartoon rendering describes elementary transition mechanisms showing F-actin domains in red, with brown regions representing low-density actin background. (*a*I–*a*IV) Four different transition mechanisms in a reference snapshot that affect the number of clusters in the following snapshot. (*b*) Pie charts showing the percentage of transitions observed throughout the trajectory at different Arp2/3 concentrations. The size of the pie chart is proportional to the total number of transitory events. (Fig. S6 shows data from entire trajectory in addition to specific time ranges as bar graph along with the standard deviation) (*c* and *d*) Estimation of (*c*) drift and (*d*) drift-corrected diffusion coefficients (bottom row) at various cluster sizes from trajectories of high Arp2/3 concentrations, 25 (left column) and 50 nM (right column) show how the instantaneous change (drift) and spread in number of domains (diffusion coefficient) depends on the number of domains present in the snapshot. (*b–d*) Entire trajectories of all replicates corresponding to each of the Arp2/3 concentrations are employed to compute these results. To see this figure in color, go online.

understand the mechanism by which high-density actin domains evolve, we studied the trajectories of the density field. We classified each domain's birth as either coming from a domain-splitting or domain-nucleation event and the loss of a domain as resulting from either domain-domain merge or domain-destruction event (Fig. 7 *a*). While domain nucleation happens when actin in a region within the reaction volume condenses above the chosen threshold, destruction happens as actin in a high-density domain relaxes from events such as myosin/crosslinker unbinding, thereby lowering actin concentration to below our chosen threshold. Fig. 7 *b* shows that increasing Arp2/3 concentration increases the frequency of occurrence for all four elementary events that alter domain number. It is interesting to note that the mechanisms that lead to an increase in domain number are roughly as prevalent as mechanisms that cause a decrease in domain number. Also, we see that among the two processes that lead to increase in domain number, namely domain splitting and domain nucleation, the former is more probable. Similarly, the reduction in number of domains between two consecutive snapshots is more often due to domain-domain merges than domain-destruction events. The probability of split and merge events as a function of minimum distance between domains (Fig. S7) shows that at [Arp2/3] = 25 and 50 nM, the domain-split and -merge events primarily happen between domains that are $\lesssim$200 nm from one another and that the probability quickly falls at larger distances. This suggests that domains reassort only when their boundaries are spatially close and that long-range interaction of domains via background, unincorporated actin is minimal.

To understand the differences in domain dynamics between networks from low and high Arp2/3 concentrations, we plotted distributions of domain-number-altering events accumulated over 500-s intervals (Fig. S6). We see that at low Arp2/3 concentrations, the high-density actin domains are highly dynamic in the first 500 s of trajectories.

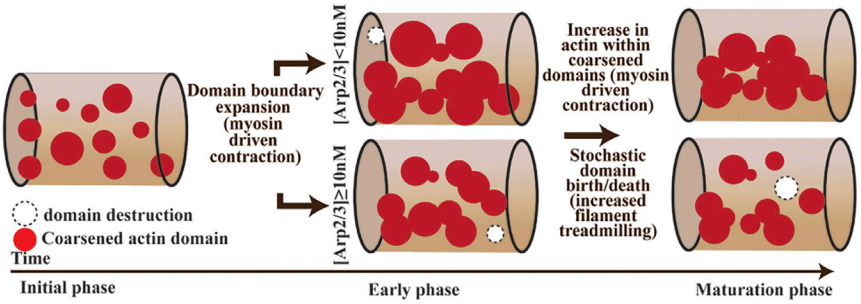

FIGURE 8 Cartoon of the proposed mechanism to explain Arp2/3-dependent network organization at micron-length scale. Cylindrical reaction volumes are shown with red blobs representing high-density actin domains. The dominant mechanism for transitions along a trajectory is mentioned, along with the filament level interaction mentioned within parenthesis. Domain destruction events are mentioned as empty circles with dotted lines. To see this figure in color, go online.

Although all four domain-birth and -death mechanisms occur, domain-domain-merge events happen at a higher frequency. As a result, within the first 500 s of trajectories, networks with [Arp2/3] $<$ 10 nM experience a steady decrease in the number of domains, resulting in a single, connected domain. The space-spanning domain is significantly less dynamic, suggesting that domain merges are irreversible in networks with low Arp2/3 concentration. This observation is consistent with experiments where actin condensates merge irreversibly with time, causing a steady increase in actin mass within condensates (4,47).

On the other hand, networks with high Arp2/3 concentrations are more dynamic than their low Arp2/3 counterparts. As the domain-birth and -death events roughly balance each other throughout the trajectories, we postulate that elevated Arp2/3 levels stochastically favor a fragmented network state with multiple, high-density actin domains. To investigate this, we employed a stochastic modeling framework assuming that the change in the number of domains in a given time interval depends on a combination of effective drift and random fluctuations (48). Further, we consider that the effective drift and diffusion terms depend on the number of domains at a given time point, N(t). Drift measures the mean number of domains in the system at time t+1, when N(t) = n. Positive (negative) drift indicates that the number of domains increases (decreases) at time t+1 when compared with N(t). Additionally, the drift-corrected diffusion coefficient measures the squared fluctuation of the of the deviation of N(t+1)-n from the drift A(n,t). Thus, a drift-corrected diffusion coefficient of zero suggests that the number of high-density domains are constant, while a large diffusion coefficient indicates high variability in N(t+1). Please refer to the supporting material for a discussion on the stochastic model and parameter estimation. Analyzing timeseries of the number of domains from trajectories, we see that the drift is lowest for states with an intermediate level of fragmentation, with minimum drift when the snapshot has three, four, and five fragmented domains for networks at 25 nM [Arp2/3] and three to six domains for 50 nM [Arp2/3] (Fig. 7 *c*). Also, for networks with more than six domains, the drift parameter is negative, indicating that the system favors domain-death events, while at values lower than the minima, drift is positive, suggesting that the system favors the birth events. Thus, the fragmented state is the result of a balance of domain dynamics. We also see that the drift-corrected diffusion coefficient term is significant at all domain number values studied (Fig. 7 *d*), highlighting the role that random noise plays in the process and leading to enhanced variability.

Relative roles of geometric branching versus kinetic nucleation in the effect of Arp2/3

The fragmentation of networks in our simulations can be explained as a combination of two distinct phenomena: myosin-driven contractility and Arp2/3-driven nucleation. We find that increasing dendritic activity in a network results in short filaments ($<$1 μm) (Fig. 1 *a*). In a parallel analysis (presented elsewhere; (43)), we find that short filaments such as these organize into a non-percolated network through which myosin-driven contractile forces cannot propagate effectively. Such non-percolated networks contract locally due to myosin-driven contractility, resulting in a fragmented network with multiple high-density actin domains, as observed above.

Arp2/3-driven nucleation of an offspring filament can be viewed as the combination effect of a minus-end-bound nucleator (similar to leiomodin (6)) and an angle-sensitive filament-filament crosslinker. To understand the relative importance of these two mechanisms, we simulated actin networks with varying concentrations of synthetic minus-end nucleators with the same kinetics as Arp2/3 but lacking the capacity to bind a mother filament and generate a branched structure. These nucleators nucleate filaments and stay attached to the minus end until unbinding. The resulting networks have distributions of filament lengths, treadmilling rate, and total number of filaments consistent with those reported above for a branching nucleator (Fig. S8 *a–c*). Analyzing the density fields at 40-μM threshold, we also find that high nucleator concentrations reproduced the network fragmentation seen with a branching nucleator (Fig. S4 *d*), suggesting that the nucleation activity alone, independent of a branching geometry, is sufficient to generate network fragmentation. Nevertheless, we see interesting quantitative differences in the organization of high-density actin domains between the two nucleators studied in a [nucleator]-dependant manner. While the number of

domains initially (<200 s) decreases with time for all nucleator concentrations, and it remains low at [nucleator] ≤ 10 nM (both Arp2/3 and synthetic minus-end nucleator) (Fig. S8 *d*), we see that differences in Arp2/3 concentration consistently exhibit more extreme effects on large-scale actin distribution than do differences in the concentration of the non-branching nucleator. Thus, we observe higher actin concentrations inside domains at low [Arp2/3], but lower concentrations at high [Arp2/3], than with the equivalent levels of the synthetic nucleator (Fig. S8 *e*). Similarly, we see a higher fraction of F-actin contained in the domains at low Arp2/3 than low nucleator (≤10 nM), but a lower fraction at high (25 nM) Arp2/3 (Fig. S8 *f*) (though at the highest level of nucleator, 50 nM, the variance becomes too large for comparison). Additionally, at higher nucleator concentrations (25 and 50 nM), Arp2/3 trajectories fragment into a higher number of domains than the synthetic minus-end nucleators. These results suggest that the branching nature of Arp2/3 enhances the sensitivity of large-scale actin organization to changes in the protein's level and activity. It may be that as Arp2/3 nucleation reinforces actin closer to regions with preexisting filaments, we see enhanced local actin concentration, leading to higher F-actin concentration in domains at low [Arp2/3] and a higher number of domains at higher [Arp2/3].

DISCUSSION

We studied the influence of Arp2/3 in tuning the micron-scale spatial organization of actin using MEDYAN, a mechano-chemical forcefield that simulates the stochastic time evolution of cytoskeletal networks. Analyzing filament-level data and density fields resulting from 2000-s-long simulations of actin networks at various Arp2/3 concentrations, we found that network organization depends on the interaction between Arp2/3-dependent actin fragmentation and myosin-dependent contractility (Fig. 8). At a given myosin concentration, the nucleation activity and finite-bound lifetime of Arp2/3 lead to an overall reduction in filament length and diversity when we increase Arp2/3. Thus, at low or intermediate Arp 2/3 concentrations (e.g., 1–10 nM), actin networks are composed of mixed populations of long (≥1 μm) and short filaments (<1 μm). In contrast, at high Arp2/3 (e.g., 50 nM), the network consists almost exclusively of short, sub-micron filaments. These changes at the filament level, when coupled with the effects of myosin activity, at elevated Arp2/3, lead to a network organization where actin is organized into separated spatial domains due to the reduced connectivity of a network composed of short filaments. In contrast, the long actin filaments presented at lower Arp2/3 concentrations allow the actin to form a single, connected, globally contractile network. In essence, actin networks become kinetically trapped in a spatially fragmented state in networks with high Arp2/3 activity due to the difference in the spatial range over which contractility can operate.

The similar but interacting effects of Arp2/3-dependent fragmentation and myosin-dependent contractility are perhaps demonstrated most clearly by their temporally segregated effects on the time evolution of the network. On short timescales (≤500 s), our analyses show that actin organization is determined primarily by myosin-driven contractility (Fig. 5). During this phase, myosin activity brings filaments closer to one another, leading to delocalized contractility of the entire actin network at all Arp2/3 concentrations studied in this work. The impact of Arp2/3 then becomes apparent at longer timescales, where the progressive reduction of average filament length causes the network to fragment into separately contractile domains. Therefore, networks with low Arp2/3 activity, having a sizable population of long filaments, continue contracting globally, generating a single domain with an actin concentration about an order of magnitude above bulk (>100 μM). At high Arp2/3 concentrations, in contrast, networks stochastically lose global connectivity and instead exhibit enhanced localized contractility that favors a fragmented state composed of multiple, separated domains.

In this work, we find that both reductions in myosin and increase in Arp2/3 favor fragmented network organization, but the nature of their effects depends on the absolute level of both. Specifically, myosin plays a substantial role in determining fragmentation of actin networks at low Arp2/3 conditions, while at elevated Arp2/3, myosin has less of an impact. Thus, reducing myosin by 50% relative to our starting baseline significantly increases network fragmentation at all Arp2/3 concentrations analyzed. In contrast, further decrease of myosin to 10% of its baseline at the starting level only increases fragmentation of low [Arp2/3] networks (≤10 nM) and has no further effect on high [Arp2/3] networks. In essence, the data suggest that the effectiveness of myosin becomes saturated as the Arp2/3 level is increased and the mean actin filament length decreases. Stated otherwise, while contractile forces of myosin are crucial to organize actin filaments into high-density domains, the efficacy of that condensation is limited by the shortening of actin filaments caused by Arp2/3. We also note that increasing Arp2/3 at any given myosin concentration gives a broader variance of actin organization patterns (range: 1–15 domains; median values), while altering myosin at any Arp2/3 has a milder impact on the number of high-density actin domains. Transitions to fragmented network states similar to those we describe have been observed experimentally (4,23). They have also been explained computationally for linear actin networks as either a sol-gel transition or coarsening-driven domain growth processes (1,4,19,23,24).

How dynamic are the high-density actin domains we observe in our simulations? To address this question, we have to discriminate between two different levels of actin

organization. At the microscopic level, at all Arp2/3 concentrations, we see that individual actin monomers and filament segments are constantly exchanged between contractile domains. At the mesoscopic level (0.5–5 μm), we observe more complex and more interesting dynamics that depend on the activity of Arp2/3 and that are likely to have significant implications for downstream biological processes. At low concentrations of Arp2/3, the entire network quickly collapses into a single, connected, contractile domain whose properties remain relatively static over time despite the continual exchange of molecular components. At somewhat higher concentrations of Arp2/3, however, a fragmented network state emerges from the underlying actin network, and it remains highly dynamic at the multi-micron level of resolution. These domains have a wide range of volumes, they merge and split continually, and they continue to exchange actin with both the neighboring domains and background actin (actin below threshold concentration). The actin network in this condition can be thought of as being in a metastable state, where, at any given Arp2/3 concentration, the network drifts stochastically toward a preferred level of fragmentation.

At the elevated levels of Arp2/3 investigated here, the network shows diffusion across a broad range of domain sizes and numbers, even at steady state. We believe that the properties of these high-density domains, such as their contractility and inter-domain dynamics, are representative of the actin network as a whole as they contain the large majority of total actin in the volume (>80% at 20 μM threshold and >50% at 40 μM threshold, relative to the 20-μM bulk concentration of actin in the simulation) and inform us of the principles of actin organization at a multi-micron spatial scale that is relevant to the processes occurring in cells. In this analysis, we chose to compute the density fields at a 100-nm-length scale due to its concordance with physical properties of actin used in our computational method. We note, however, that it is also not so different from the resolution of typical fluorescent imaging experiments. As a result, it offers us the possibility of validating the biological relevance of our computational observations by comparing our results with experimental observations (29,30). Indeed, in a study we have recently presented elsewhere (43), we have shown that the simulations investigated here, together with additional, related simulations, generate mesoscopic patterns of actin distribution that effectively mimic the actin distributions observed experimentally by quantitative live imaging of single axonal growth cones *in vivo* in the developing *Drosophila* wing (30,43).

One possible implication from our analysis is that the limited lifetime of the parent-Arp2/3-offspring filament complex may significantly affect the hierarchical organization of actin from sub-micron- to micron-length scales. Diffusing Arp2/3 complexes modeled in our simulations are treated as active and readily bind to the sides of parent filaments to generate offspring filaments. Upon unbinding, Arp2/3 molecules are released and can bind to a new filament and continue to nucleate offspring filaments.(49) Thus, the finite-bound lifetime of Arp2/3 (42) presumably contributes to an enhanced nucleation rate, particularly at higher Arp2/3 concentrations, and promotes overall reduction in filament lengths. However, Arp2/3 molecules modeled with infinite-bound lifetimes have been shown to accumulate significant stresses in the network that are released instantaneously, causing large deformations in a mechanism similar to avalanches (28,50). As the branches in our study unbind at with a 50-s residence time (42), we do not observe such large deformations in the force-sensitive unbranching model used in the current work. It remains to be seen if our networks exhibit non-Gaussian stress-relaxation patterns in a phenomenon similar to cytoquakes found in other studies (18,51–54), and if not, does that contribute to the domain dynamics that we observe.

Perhaps surprisingly, by performing simulations in which we model the nucleating activity of Arp2/3 but remove its branching function, we find that the nucleation activity of Arp2/3 alone is sufficient to reproduce the spatial fragmentation patterns observed under Arp2/3 conditions, even in the absence of a dendritic branching geometry. Thus, we believe that our findings here could be relevant to other actin nucleators as well. These findings are critical to understanding the relationship between network architecture and functional consequence in filamentous biological active matter by separating the contributions of network dynamics from those of network geometry (2,55,56).

The ability of actin modifiers to alter actin architecture from the sub-micron to the multi-micron level has critical implications for biological systems. For example, we hypothesize that under such fragmented conditions, actin networks can work cooperatively with transport myosins such as Myosin V (57) and Myosin X (58) to create spatially diverse and disconnected fluxes of critical biological molecules within a single cytoplasm. Moreover, we hypothesize that the emergent property of a fragmented cellular cytoskeleton under high Arp2/3 activity may facilitate local responses to signaling cues within small, kinetically confined domains (59,60). In contrast, the connected networks generated at low Arp2/3 concentrations may favor a unitary response involving the entire cytoplasmic network over multi-micron-length scales (61–63). Additionally, network remodeling between the globally connected versus fragmented states can be crucial to modulate both the intensity and spatial range of signaling processes and morphological transitions. We suggest that cells may employ changing levels of Arp2/3 activity to tune the network between connected and fragmented states of actin to reorganize the structural and, as a result, functional roles of the cytoskeleton.

CONCLUSION

Our work demonstrates how large-scale actin network organization can be drastically altered by the presence of the

branching nucleator, Arp2/3. Changing the concentration of Arp2/3 alters overall network connectivity by altering the proportion of sub-micron-long filaments. We show that irrespective of Arp2/3 concentration, networks initially ($t < 100$ s) evolve with localized contraction, leading to multiple domains of condensed actin. As the network evolves, we initially observe contractile domain-merge events, resulting in fewer actin domains. As network evolution progresses, we see that networks with low Arp2/3 activity are trapped in the connected, globally contractile state. In contrast, high Arp2/3 activity promotes domain-level processes that cause the networks to evolve stochastically toward fragmented network states. This study suggests that signaling pathways that affect Arp2/3 levels tune the overall network architecture, switching between a globally coherent state versus a fragmented state with enhanced local responsiveness.

DATA AVAILABILITY

The details of MEDYAN model implementation can be accessed online (https://github.com/medyan-dev/medyan-public), and a link to the source code can be found under the releases tab of the repository.

The analysis scripts used for this study and the input files can be found at https://github.com/achansek/readMEDYANtraj and https://github.com/achansek/MEDYANArp23_2021.

SUPPORTING MATERIAL

Supporting material can be found online at https://doi.org/10.1016/j.bpj.2022.07.035.

AUTHOR CONTRIBUTIONS

A.C., E.G., and G.A.P. designed research; A.C. performed research; A.C. and G.A.P. contributed analytical tools; A.C. analyzed data; A.C., E.G., and G.A.P wrote the manuscript.

ACKNOWLEDGMENTS

We would like to thank Carlos Floyd, Haoran Ni, Qin Ni, and Ashwin Ravichandran for their helpful feedback. This work was supported in part by NSF CHE-1800418 and CHE-2102684 and by the Intramural Research Program of NINDS, NIH, grant Z01-NS003013 to E.G. MEDYAN simulations were carried out on the Deepthought2 Supercomputer at the University of Maryland and the Biowulf Supercomputer at the National Institutes of Health.

DECLARATION OF INTERESTS

The authors declare no competing interests.

REFERENCES

1. Alvarado, J., M. Sheinman, …, G. H. Koenderink. 2013. Molecular motors robustly drive active gels to a critically connected state. *Nat. Phys.* 9:591–597.
2. Koenderink, G. H., and E. K. Paluch. 2018. Architecture shapes contractility in actomyosin networks. *Curr. Opin. Cell Biol.* 50:79–85.
3. Sonal, K. A., K. A. Ganzinger, …, P. Schwille. 2019. Myosin-II activity generates a dynamic steady state with continuous actin turnover in a minimal actin cortex. *J. Cell Sci.* 132
4. Soares E Silva, M., M. Depken, …, G. H. Koenderink. 2011. Active multistage coarsening of actin networks driven by myosin motors. *Proc. Natl. Acad. Sci. USA.* 108:9408–9413.
5. Hannezo, E., B. Dong, …, S. Hayashi. 2015. Cortical instability drives periodic supracellular actin pattern formation in epithelial tubes. *Proc. Natl. Acad. Sci. USA.* 112:8620–8625.
6. Firat-Karalar, E. N., and M. D. Welch. 2011. New mechanisms and functions of actin nucleation. *Curr. Opin. Cell Biol.* 23:4–13.
7. Bovellan, M., Y. Romeo, …, G. Charras. 2014. Cellular control of cortical actin nucleation. *Curr. Biol.* 24:1628–1635.
8. Swaney, K. F., and R. Li. 2016. Function and regulation of the Arp2/3 complex during cell migration in diverse environments. *Curr. Opin. Cell Biol.* 42:63–72.
9. Mullins, R. D., J. A. Heuser, and T. D. Pollard. 1998. The interaction of Arp2/3 complex with actin: nucleation, high affinity pointed end capping, and formation of branching networks of filaments. *Proc. Natl. Acad. Sci. USA.* 95:6181–6186.
10. Pollard, T. D. 2007. Regulation of actin filament assembly by Arp2/3 complex and formins. *Annu. Rev. Biophys. Biomol. Struct.* 36:451–477.
11. Goley, E. D., and M. D. Welch. 2006. The ARP2/3 complex: an actin nucleator comes of age. *Nat. Rev. Mol. Cell Biol.* 7:713–726.
12. Pollitt, A. Y., and R. H. Insall. 2009. WASP and SCAR/WAVE proteins: the drivers of actin assembly. *J. Cell Sci.* 122:2575–2578.
13. Molinie, N., and A. Gautreau. 2018. The Arp2/3 regulatory system and its deregulation in cancer. *Physiol. Rev.* 98:215–238.
14. Padrick, S. B., and M. K. Rosen. 2010. Physical mechanisms of signal integration by WASP family proteins. *Annu. Rev. Biochem.* 79:707–735.
15. Tyler, J. J., E. G. Allwood, and K. R. Ayscough. 2016. WASP family proteins, more than Arp2/3 activators. *Biochem. Soc. Trans.* 44:1339–1345.
16. Rotty, J. D., C. Wu, and J. E. Bear. 2013. New insights into the regulation and cellular functions of the ARP2/3 complex. *Nat. Rev. Mol. Cell Biol.* 14:7–12.
17. Papalazarou, V., and L. M. Machesky. 2021. The cell pushes back: the Arp2/3 complex is a key orchestrator of cellular responses to environmental forces. *Curr. Opin. Cell Biol.* 68:37–44.
18. Floyd, C., G. A. Papoian, and C. Jarzynski. 2019. Quantifying dissipation in actomyosin networks. *Interface Focus.* 9:20180078–20180110.
19. Alvarado, J., M. Sheinman, …, G. H. Koenderink. 2017. Force percolation of contractile active gels. *Soft Matter.* 13:5624–5644.
20. Mulla, Y., F. C. Mackintosh, and G. H. Koenderink. 2019. Origin of slow stress relaxation in the cytoskeleton. *Phys. Rev. Lett.* 122:218102.
21. Lieleg, O., J. Kayser, …, A. R. Bausch. 2011. Slow dynamics and internal stress relaxation in bundled cytoskeletal networks. *Nat. Mater.* 10:236–242.
22. Stricker, J., T. Falzone, and M. L. Gardel. 2010. Mechanics of the F-actin cytoskeleton. *J. Biomech.* 43:9–14.
23. Weirich, K. L., S. Banerjee, …, M. L. Gardel. 2017. Liquid behavior of cross-linked actin bundles. *Proc. Natl. Acad. Sci. USA.* 114:2131–2136.
24. Weirich, K. L., K. Dasbiswas, …, M. L. Gardel. 2019. Self-organizing motors divide active liquid droplets. *Proc. Natl. Acad. Sci. USA.* 116:11125–11130.
25. Bendix, P. M., G. H. Koenderink, …, D. A. Weitz. 2008. A quantitative analysis of contractility in active cytoskeletal protein networks. *Biophys. J.* 94:3126–3136.
26. Haase, K., and A. E. Pelling. 2013. The role of the actin cortex in maintaining cell shape. *Commun. Integr. Biol.* 6:e26714.

27. Ni, Q., and G. A. Papoian. 2019. Turnover versus treadmilling in actin network assembly and remodeling. *Cytoskeleton.* 76:562–570.
28. Liman, J., C. Bueno, …, M. S. Cheung. 2020. The role of the Arp2/3 complex in shaping the dynamics and structures of branched actomyosin networks. *Proc. Natl. Acad. Sci. USA.* 117:10825–10831.
29. Clarke, A., P. G. McQueen, …, E. Giniger. 2020. Abl signaling directs growth of a pioneer axon in Drosophila by shaping the intrinsic fluctuations of actin. *Mol. Biol. Cell.* 31:466–477.
30. Clarke, A., P. G. McQueen, …, E. Giniger. 2020. Dynamic morphogenesis of a pioneer axon in Drosophila and its regulation by Abl tyrosine kinase. *Mol. Biol. Cell.* 31:452–465.
31. Popov, K., J. Komianos, and G. A. Papoian. 2016. Medyan : mechanochemical simulations of contraction and polarity alignment in actomyosin networks. *PLoS Comput. Biol.* 12. e1004877.
32. Gibson, M. A., and J. Bruck. 2000. Efficient exact stochastic simulation of chemical systems with many species and many channels. *J. Phys. Chem. A.* 104:1876–1889.
33. Chandrasekaran, A., A. Upadhyaya, and G. A. Papoian. 2019. Remarkable structural transformations of actin bundles are driven by their initial polarity, motor activity, crosslinking, and filament treadmilling. *PLoS Comput. Biol.* 15. e1007156.
34. Li, X., Q. Ni, …, Y. Jiang. 2020. Tensile force-induced cytoskeletal remodeling: mechanics before chemistry. *PLoS Comput. Biol.* 16. e1007693.
35. Ni, Q., K. Wagh, …, G. A. Papoian. 2021. A tug of war between filament treadmilling and myosin induced contractility generates actin cortex. Preprint at bioRxiv. https://doi.org/10.1101/2021.06.06.447254.
36. Komianos, J. E., and G. A. Papoian. 2018. Stochastic ratcheting on a funneled energy landscape is necessary for highly efficient contractility of actomyosin force dipoles. *Phys. Rev. X.* 8:021006.
37. Faust, J. J., B. A. Millis, and M. J. Tyska. 2019. Profilin-mediated actin allocation regulates the growth of epithelial microvilli. *Curr. Biol.* 29:3457–3465.e3.
38. Ott, A., M. Magnasco, …, A. Libchaber. 1993. Measurement of the persistence length of polymerized actin using fluorescence microscopy. *Phys. Rev. E.* 48:R1642–R1645.
39. Kojima, H., A. Ishijima, and T. Yanagida. 1994. Direct measurement of stiffness of single actin filaments with and without tropomyosin by in vitro nanomanipulation. *Proc. Natl. Acad. Sci. USA.* 91:12962–12966.
40. Han, X., Y. Su, …, H. Shroff. 2021. A polymer index-matched to water enables diverse applications in fluorescence microscopy. *Lab Chip.* 21:1549–1562.
41. Svitkina, T. M., and G. G. Borisy. 1999. Arp2/3 complex and actin depolymerizing factor/cofilin in dendritic organization and treadmilling of actin filament array in lamellipodia. *J. Cell Biol.* 145:1009–1026.
42. Mahaffy, R. E., and T. D. Pollard. 2006. Kinetics of the formation and dissociation of actin filament branches mediated by Arp2/3 complex. *Biophys. J.* 91:3519–3528.
43. Chandrasekaran, A., A. Clarke, …, E. Giniger. 2021. Computational simulations reveal that Abl activity controls cohesiveness of actin networks in growth cones. *Mol. Biol. Cell.* 33:mbcE21110535.
44. Fujiwara, I., S. Suetsugu, …, S. Ishiwata. 2002. Visualization and force measurement of branching by Arp2/3 complex and N-WASP in actin filament. *Biochem. Biophys. Res. Commun.* 293:1550–1555.
45. Paciolla, M., D. J. Arismendi-Arrieta, and A. J. Moreno. 2020. Coarsening kinetics of complex macromolecular architectures in bad solvent. *Polymers.* 12:5311–E620.
46. Testard, V., L. Berthier, and W. Kob. 2014. Intermittent dynamics and logarithmic domain growth during the spinodal decomposition of a glass-forming liquid. *J. Chem. Phys.* 140:164502.
47. Hu, S., K. Dasbiswas, …, A. D. Bershadsky. 2017. Long-range self-organization of cytoskeletal myosin II filament stacks. *Nat. Cell Biol.* 19:133–141.
48. Gardiner, C. W. 2009. Stochastic Methods A Handbook for the Natural and Social Sciences. Springer-Verlag Berlin Heidelberg.
49. Millius, A., N. Watanabe, and O. D. Weiner. 2012. Diffusion, capture and recycling of SCAR/WAVE and Arp2/3 complexes observed in cells by singlemolecule imaging. *J. Cell Sci.* 125:1165–1176.
50. Li, C., J. Liman, …, M. S. Cheung. 2021. Forecasting avalanches in branched actomyosin networks with network science and Machine learning. *J. Phys. Chem. B.* 125:11591–11605.
51. Shi, Y., C. L. Porter, …, D. H. Reich. 2019. Dissecting fat-tailed fluctuations in the cytoskeleton with active micropost arrays. *Proc. Natl. Acad. Sci. USA.* 116:13839–13846.
52. Alencar, A. M., M. S. A. Ferraz, …, J. P. Butler. 2016. Non-equilibrium cytoquake dynamics in cytoskeletal remodeling and stabilization. *Soft Matter.* 12:8506–8511.
53. Floyd, C., H. Levine, …, G. A. Papoian. 2021. Understanding cytoskeletal avalanches using mechanical stability analysis. *Proc. Natl. Acad. Sci. USA.* 118. e2110239118.
54. Toyota, T., D. A. Head, …, D. Mizuno. 2011. Non-Gaussian athermal fluctuations in active gels. *Soft Matter.* 7:3234–3239.
55. Letort, G., A. Politi, …, L. Blanchoin. 2014. Geometrical and mechanical properties control actin filament organization. *Biophys. J.* 106:568a–569a.
56. Reymann, A. C., J. L. Martiel, …, M. Théry. 2010. Nucleation geometry governs ordered actin networks structures. *Nat. Mater.* 9:827–832.
57. Kodera, N., D. Yamamoto, …, T. Ando. 2010. Video imaging of walking myosin v by high-speed atomic force microscopy. *Nature.* 468:72–76.
58. Berg, J. S., and R. E. Cheney. 2002. Myosin-X is an unconventional myosin that undergoes intrafilopodial motility. *Nat. Cell Biol.* 4:246–250.
59. Moore, A. S., Y. C. Wong, …, E. L. F. Holzbaur. 2016. Dynamic actin cycling through mitochondrial subpopulations locally regulates the fission-fusion balance within mitochondrial networks. *Nat. Commun.* 7:12886.
60. McCall, P. M., S. Srivastava, …, M. V. Tirrell. 2018. Partitioning and enhanced self-assembly of actin in polypeptide coacervates. *Biophys. J.* 114:1636–1645.
61. Schaus, T. E., E. W. Taylor, and G. G. Borisy. 2007. Self-organization of actin filament orientation in the dendritic-nucleation/array-treadmilling model. *Proc. Natl. Acad. Sci. USA.* 104:7086–7091.
62. Wu, C., S. B. Asokan, …, J. E. Bear. 2012. Arp2/3 is critical for lamellipodia and response to extracellular matrix cues but is dispensable for chemotaxis. *Cell.* 148:973–987.
63. Mueller, J., G. Szep, …, M. Sixt. 2017. Load adaptation of lamellipodial actin networks. *Cell.* 171:188–200.e16.

Biophysical Journal, Volume *121*

Supplemental information

Nucleation causes an actin network to fragment into multiple high-density domains

Aravind Chandrasekaran, Edward Giniger, and Garegin A. Papoian

Nucleation causes an actin network to fragment into multiple high-density domains

Supplementary Information

Aravind Chandrasekaran[1, 2], Edward Giniger[3], Garegin A. Papoian[1, 2*]

[1] Department of Chemistry and Biochemistry, University of Maryland, College Park, Maryland, United States of America

[2] Institute for Physical Science and Technology, University of Maryland, College Park, Maryland, United States of America

[3] National Institutes of Neurological Diseases and Stroke, National Institutes of Health, Bethesda, Maryland, United States of America

*** Contact: gpapoian@umd.edu**

Supplementary Table

Parameter	Symbol	Value	Reference
Geometric parameters			
Compartment size	L_{comp}	500nm	(1)
Number of compartments in each dimension	Nx,Ny,Nz	4,4,15	-
Length of a cylinder	L_{cyl}	40 subunits (108nm)	-
Binding sites per cylinder	$N_{b,sites}$	4	-
Minifilament binding distance	$d_{NMII,bind}$	175-225nm	(1)
α-actinin binding distance	$d_{\alpha,bind}$	30-40nm	(1)
Diffusion rates			
Actin	$k_{actin,diff}$	$20\mu m^2/s$ [80 s^{-1}]	(1)
α-actinin	$k_{\alpha,diff}$	$k_{actin,diff}/10$	(1)
Myosin minifilament	$k_{NMII,diff}$	$k_{actin,diff}/100$	(1)
Enabled	$k_{Ena,diff}$	$k_{actin,diff}/100$	-
Arp2/3	$k_{Arp,diff}$	$k_{actin,diff}/100$	-
Kinetic rate constants			
Actin polymerization at plus end	$k_{actin\ poly,+}$	11.6 $(\mu M.s)^{-1}$ [0.154s^{-1}]	(2)
Actin **de**polymerization at plus end	$k_{actin\ depoly,+}$	1.3 $(\mu M.s)^{-1}$ [0.017s^{-1}]	(2)
Actin polymerization at minus-end	$k_{actin\ poly,-}$	1.4 s^{-1}	(2)
Actin **de**polymerization at minus end	$k_{actin\ depoly,-}$	0.8 s^{-1}	(2)
α-actinin binding	$k_{\alpha,bind}$	0.7 $(\mu M.s)^{-1}$ [0.009 s^{-1}]	(3)
α-actinin unbinding (F=0pN)	$k_{\alpha,unbind}$	0.3 s^{-1}	(3)
NMII head binding, minifilament binding	$k_{head,bind}$, $k_{MF,\ bind}$	0.2s^{-1}, $k_{head,bind}(N_{min+}N_{max})/2$	(4)
NMII head unbinding (F=0pN)	$k_{head,unbind}$	1.0s^{-1}	**a**

Arp2/3 binding	$k_{Arp,bind}$	$0.0017s^{-1}$	**b**(5)
Arp2/3 unbinding (F=0pN)	$k_{Arp,unbind}$	$0.02s^{-1}$	**c**(6)
Mechanochemical constants			
NMII/α-actinin binding pitch on actin filament	-	27nm	(1)
NMII head step size	d_{step}	6.0nm	**d**(7)(8)
NMII minifilament range of number of heads on each side of bipolar minifilament	N_{min}-N_{max}	$N_t \in [15, 30]$	**e**(9, 10)
NMII minifilament stall force	$F_{NMII,stall}$	300pN for minifilament	**f**
NMII per head unbinding Force	$F_{NMII,\ unbind}$	12.62pN per head	(11)
Tunable parameters	β	2.0	(1) **g**
	α	0.2	(1) **g**
Linker unbinding force	$F_{\alpha,\ unbind}$	17.2pN	(12)
Arp2/3 unbinding force	$F_{B,unbind}$	6pN	(13)
Characteristic force of Brownian ratchet	$F_{ratchet}$	1.5pN	(14)
Mechanical constants			
Actin filament stretching constant	$K_{fil,str}$	100pN/nm	(1)
Actin filament bending energy	ε_{bend}	2690pN.nm	(1)
Cylinder-Cylinder Excluded volume constant	K_{vol}	10^5pN.nm^5	(1)
Myosin cross-bridge stiffness	$K_{NMII,str}$	2.5pN/nm	(8)
α-actinin stiffness	$K_{\alpha,str}$	8pN/nm	(15)
Boundary repulsion energy	$\varepsilon_{boundary}$	$10k_BT$	-
Boundary repulsion screening length	Λ	2.7nm	-
Arp2/3 stretching constant	$K_{branch,str}$	100pN/nm	**h**
Arp2/3 bending constant, equilibrium angle	$\epsilon_{branch,bend}$, θ_o	10pN.nm, 70°	**h**
Arp2/3 bending constant #2, equilibrium angle	$\epsilon_{branch,bend,position}$, θ_o	20pN.nm, 90°	**h**
Arp2/3 dihedral constant	$\eta_{branch,dihedral}$	10pN.nm	**h**
Minimization parameters			
Length of the chemical step	$\delta_{chemistry}$	25ms	-
Force tolerance for mechanical minimization	F_T	10pN	-

Table S1 Table of simulation parameters used in MEDYANv4.1 to simulate dendritic actin networks.

aObtained by assuming a duty ratio of 17%, which is the average of the 11% duty ratio corresponding to NMIIA and 23% duty ratio corresponding to NMIIB.(4)
b Obtained from an ODE model as described in reference.
cBased on ATP actin parent filaments.
dValue chosen is close to the *Dictyostelium* step size of 7.3±0.4nm

e Experimental results suggest the total number of heads in NMIIA- 56(10), 58(9), NMIIB-60(9), and NMIIC-28(9). Here, we use a wide range to account for multiple binding modes of myosin isoforms.
f Considering the myosin-actin cross-bridge stiffness of k_{mhead} = 2.5pN/nm (8), the stall force of a single head F_{head} = $k_{mhead}xd_{step}$=15pN. If 15 heads are bound, the $F_{stall,15}$=225pN, while 30 bound heads result in $F_{stall,30}$=450pN. As our simulations dynamically choose myosin heads at binding, a stall force of about 300pN was chosen.
g α parameter tunes the force sensitivity of myosin walking rate while β tunes the force sensitive number of bound myosin heads. Please refer to Supporting Information, Supplementary Methods for a detailed description of the mathematical models used.
h Branching stretching constant is empirically chosen to restrain the distance between parent and offspring filaments. Bending constant is chosen such that the angle does not deviate from the experimentally observed standard deviation.(16, 17). The second bending potential is used to restrict the angle formed by parent cylinder plus end, binding site on parent cylinder, and offspring cylinder minus end (Figure S10) to 90°. Dihedral angle is empirically chosen to ensure parent and offspring filament binding plane is preserved.

[Arp2/3]	M:A=0.1 vs M:A=0.05	M:A=0.05 vs M:A=0.01
1	1.37×10^{-35}	0.0021
5	7.16×10^{-47}	0.0021
10	4.68×10^{-29}	0.0022
25	2.59×10^{-26}	0.87
50	0.86	1.0

Table S2. Table of p-values resulting from pair-wise Wilcoxon test. Null hypothesis is that the two distribution medians are the same and the alternate hypothesis is that the median number of domains is higher under a higher M:A ratio.

Supplementary Figures

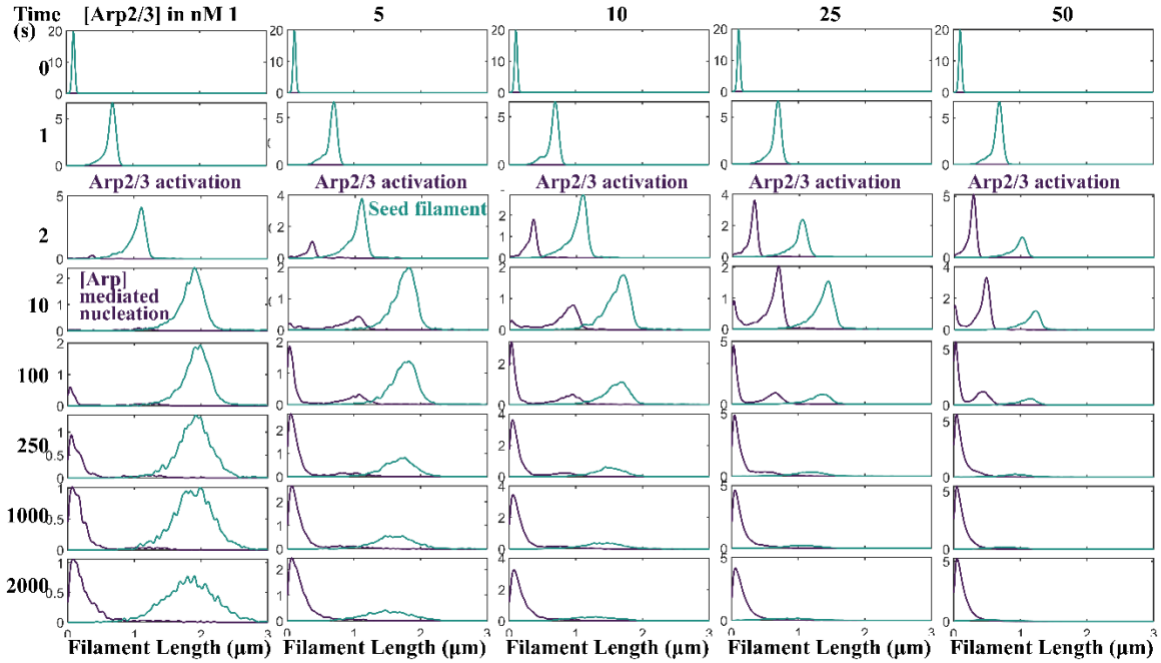

Figure S1 Arp2/3 nucleated filaments reach sub-micron length scales. Filament length distributions are shown at different time points (down each column) of the MEDYAN-generated trajectories at various Arp2/3 concentrations (left to right in each row). Arp2/3 concentrations are mentioned on the top, while simulation time in seconds is mentioned to the left of the figure. Arp2/3 activation at 1s is also shown. At any given Arp2/3 concentration and time (in other words, in any given panel), the length distribution of filaments extended from initial seeds is shown in green, while length distributions of Arp2/3 nucleated filaments are shown in purple.

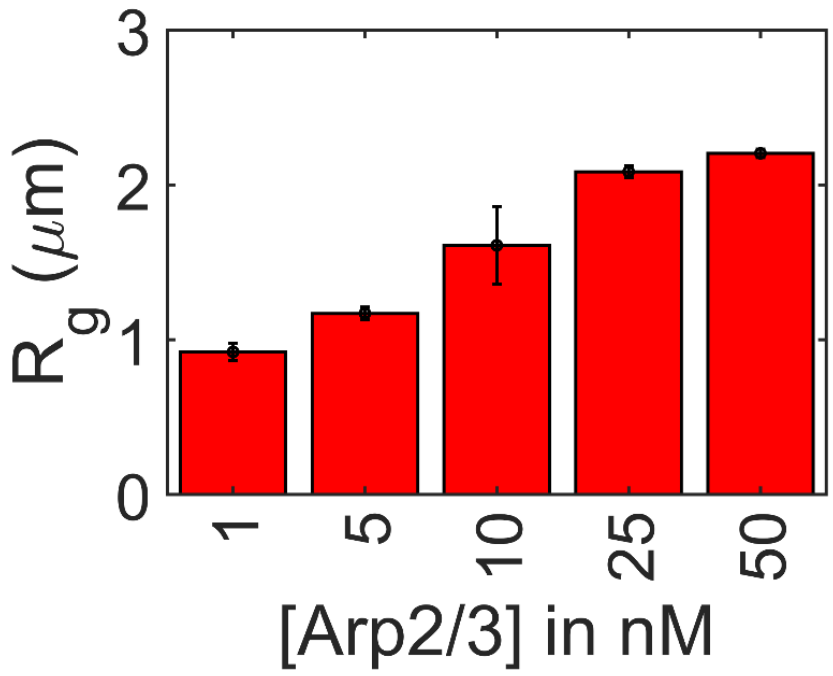

Figure S2. Radius of gyration of F-actin networks at various Arp2/3 concentrations. Mean and standard deviation of network radius of gyration from the last 500s of trajectories are shown at various Arp2/3 concentrations. We see that the network-level configurations of filamentous actin has reached steady-state. Last 500s of six replicates per [Arp2/3].

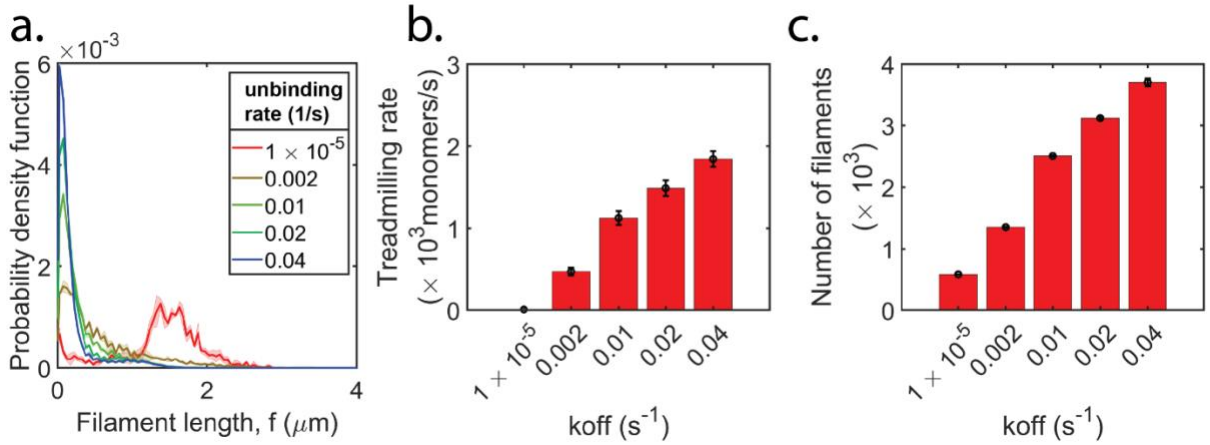

Figure S3. Variation of Arp2/3 unbinding rate shows the role of Arp2/3 residence time at [Arp2/3]=25nM. a) Mean (solid line) and standard deviation (shaded area) of filament length distribution is shown colored by Arp2/3 unbinding rate as shown in the legend. b. The mean treadmilling rate of network is shown at various Arp2/3 unbinding rates. Error bars represent standard deviation. c. The mean total number of filaments in the later part of the simulation is shown as a bar graph for various Arp2/3 unbinding rates. Error bars represent standard deviation. a-c. Data from the last 500s of 3 replicates, sampling frequency=5s.

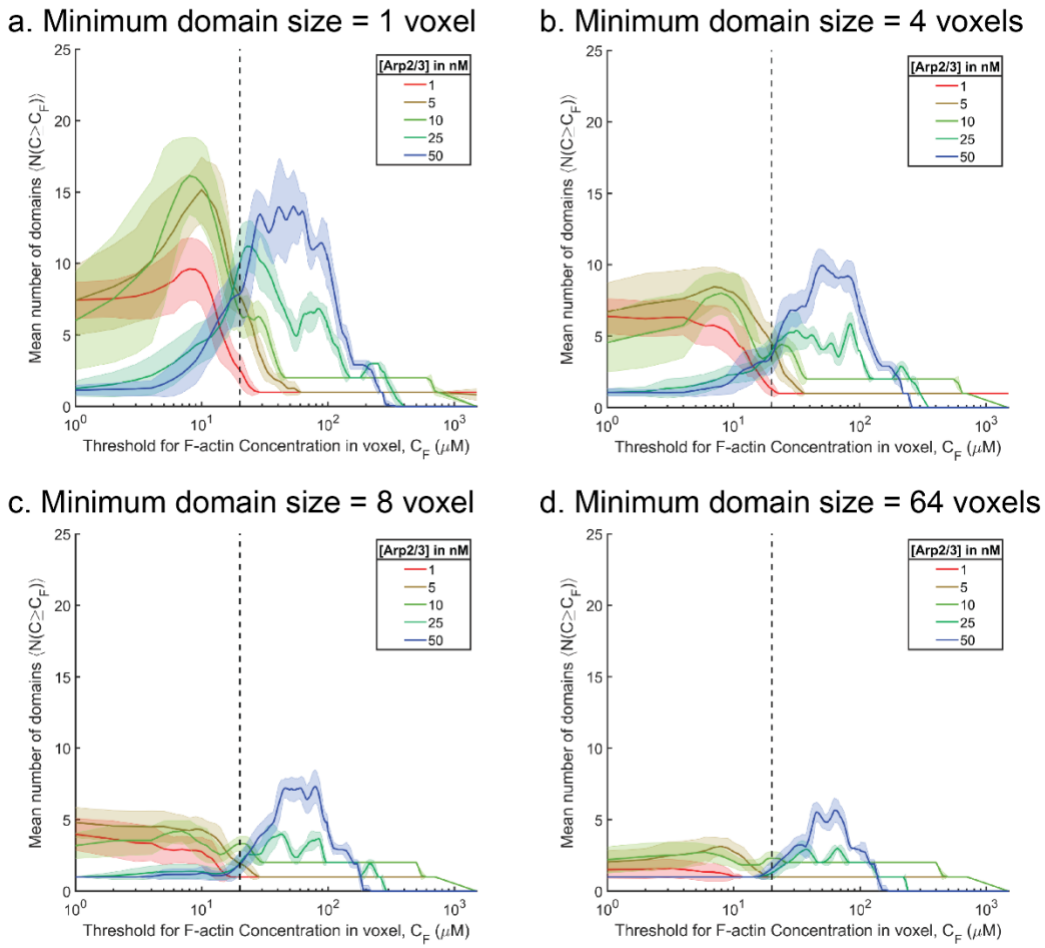

Figure S4. Domain volume threshold do not affect the qualitative trends ion number of domains at various Arp2/3 concentrations. a-d) The number of domains found in last 100s of six trajectories at various Arp2/3 concentrations (shown in legend) are shown. Solid line and shaded area represent mean and standard deviation. Dotted vertical line corresponds to bulk concentration of 20μM.

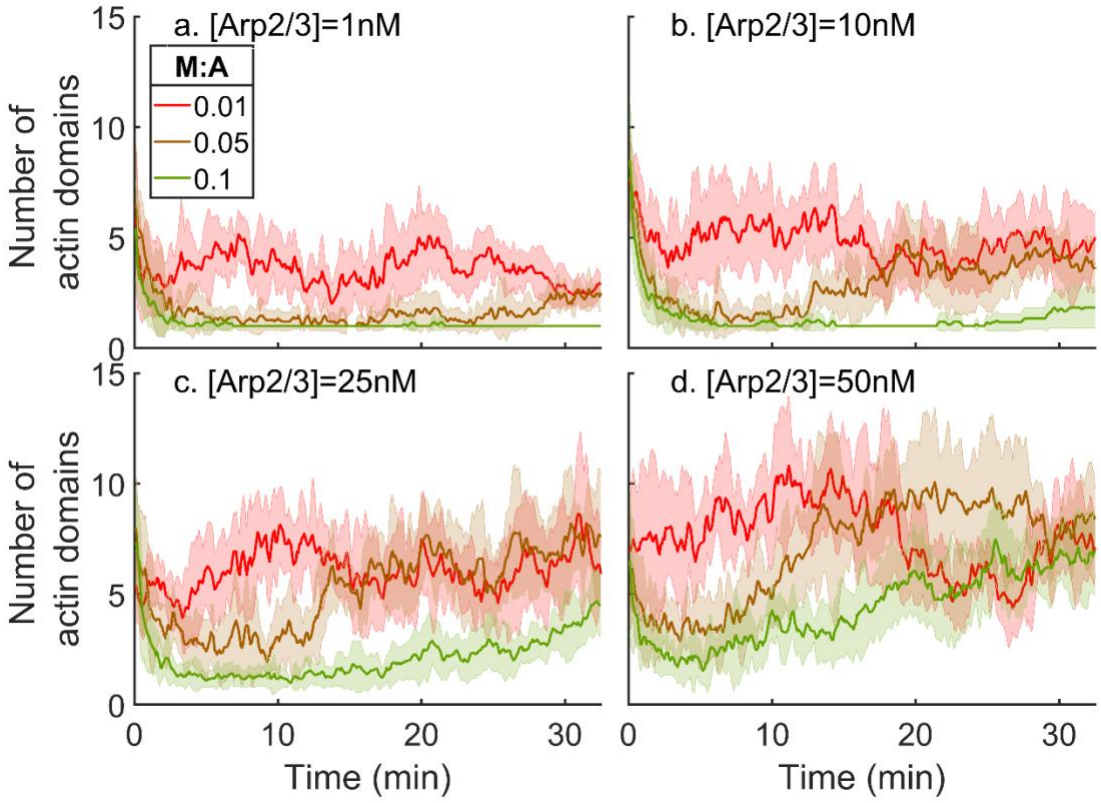

Figure S5. Influence of myosin in contractile dynamics of a dendritic network. a) Plot shows the number of domains in the actin density field obtained at a threshold concentration of 40μM at a) 1nM, b) 10nM, c) 25nM, and d) 50nM Arp2/3 concentration under three different myosin concentrations. Myosin mole ratios are mentioned in the legend. The solid line represents the mean, and the shaded area represents the standard deviation in the number of actin domains.

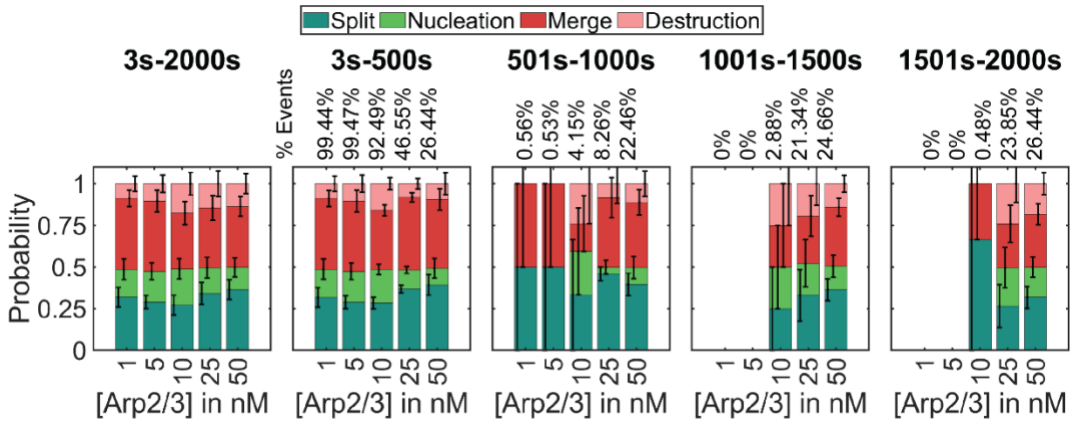

Figure S6. Distribution of different mechanisms that affect the number of high-density actin domains. Pie charts show the percentage of events that lead to birth or loss of domains. Each panel shows the probability of domain split, nucleation, merge and destruction processes along with the standard deviation across trajectories as Arp2/3 concentration is varies along timescales mentioned on the top. Under Arp2/3 concentrations of 1, and 5nM, most of the birth/death events occur in the initial 500s of the trajectories hence we see large standard deviations at later time ranges.

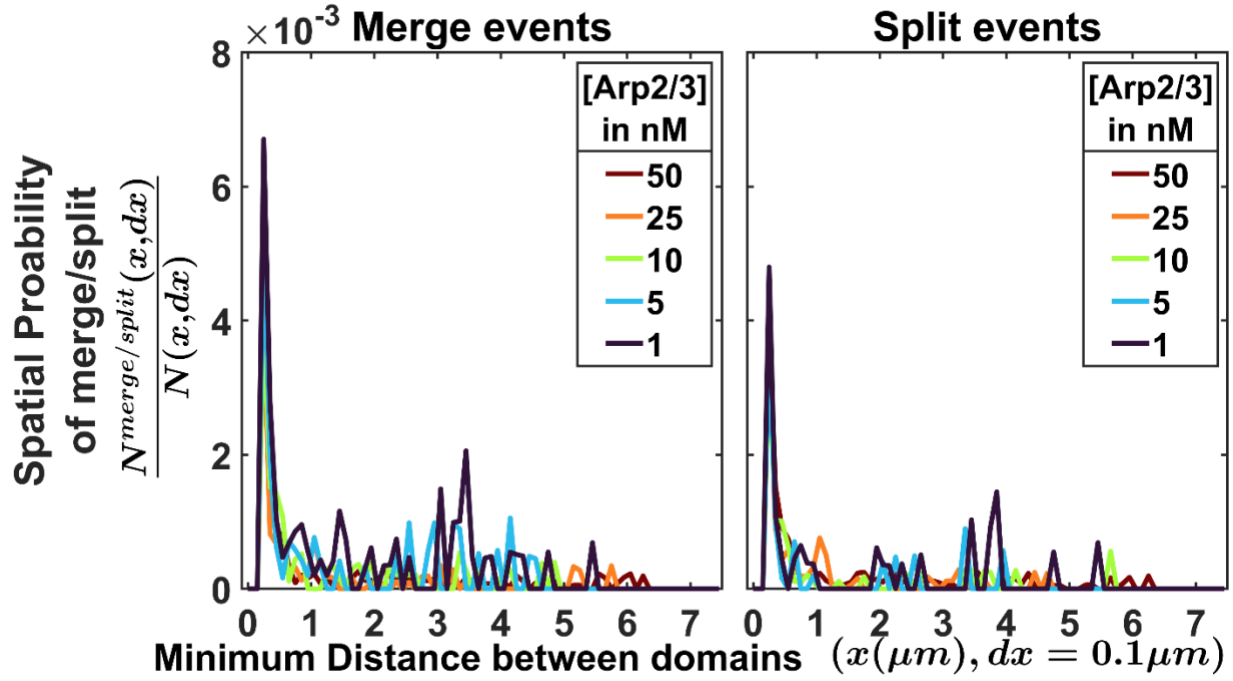

Figure S7. High-density domains are relatively weakly coupled to one another. Probabilities of split and merge events are shown as a function of distance from all time points (six replicates, sampling frequency=1s) in the trajectories. Profiles are colored according to Arp2/3 concentration shown in the legend.

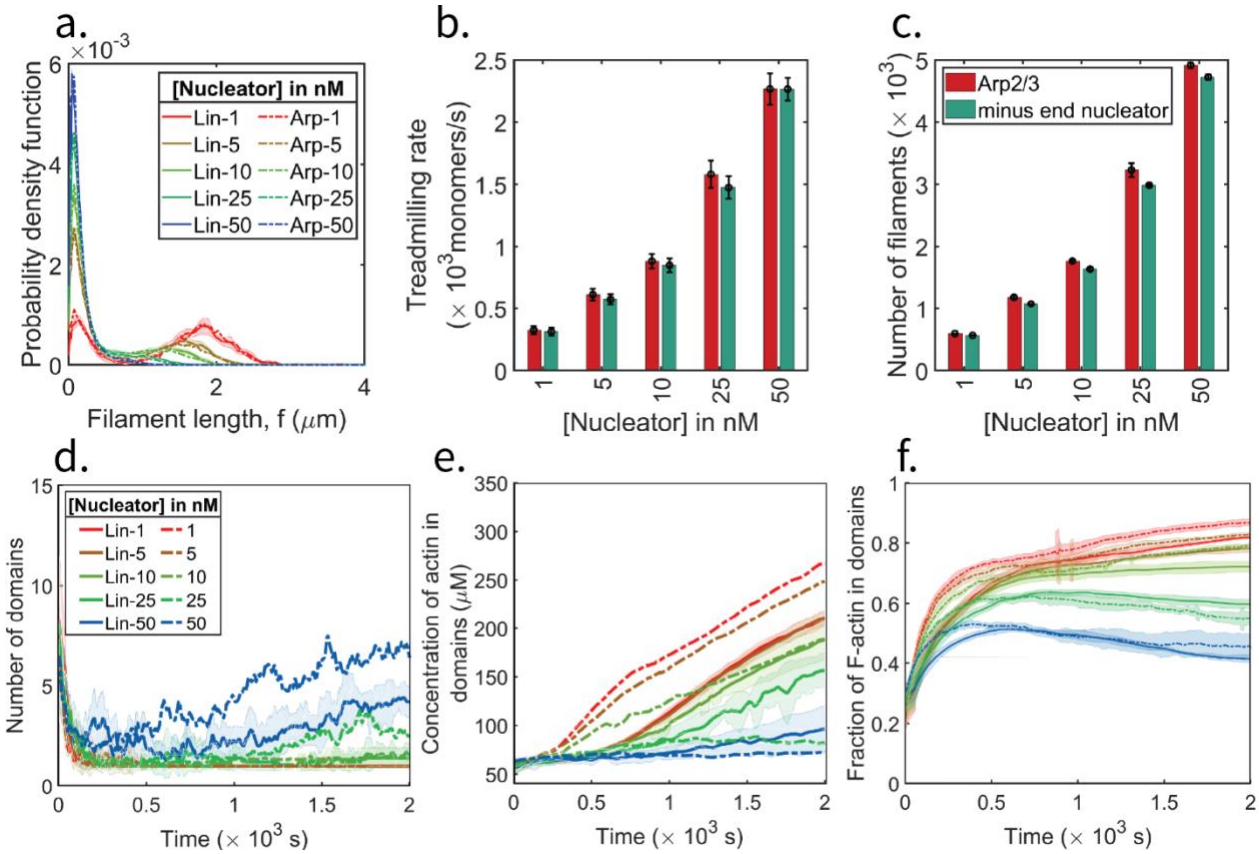

Figure S8. Linear nucleators with Arp2/3 kinetic parameters reproduces fragmentation patterns. a. Mean (solid line) and standard deviation (shaded area) of filament length distributions corresponding to trajectories with linear minus end nucleators are shown. The mean (dashed line) filament length distributions corresponding to various [Arp2/3] are also overlaid showing that both nucleators result in similar filament length distributions. Profiles are colored by nucleator concentration as shown in legend. b. Treadmilling rate from trajectories at various [Arp2/3] (red) and linear minus end nucleators (green) are shown. Error bars represent standard deviation. c. Number of filaments at the end of the simulation at various [Arp2/3] (red) and linear minus end nucleators (green) are shown. Error bars represent standard deviation. a-c. Data from the last 500s of all replicates (linear nucleators = 5, Arp2/3 = 6) was used to generate plots. Data suggests both Arp2/3 and linear minus end nucleator results in networks with similar filament length, treadmilling rate, and total number of filaments. Using 40 μM density threshold, we find the high-actin density domains in the density field. d-f. Profile line patterns and colors correspond to the nucleator type and nucleators concentration respectively as shown in the legend in panel d. d. The mean (solid line) and standard deviation (shaded area) in number of domains identified in trajectories with varying concentration of minus end nucleators is shown as a time profile. Time profiles of mean (dotted line) time profiles of number of domains in trajectories at various [Arp2/3] are also overlaid. e. The concentration of actin in the high-density actin domains from trajectories at various minus end nucleators concentrations are plotted as a time series with mean (solid) line and standard deviation (shaded area). Time profiles of mean (dotted line) actin domain concentration in trajectories with varying [Arp2/3] are also overlaid. f. The fraction of total actin in the high-density domains is plotted as time series showing mean (solid line) and standard deviation (shaded area) corresponding to trajectories at various minus end nucleators concentration. Mean time profiles (dotted line) of actin fraction computed in trajectories at varying [Arp2/3] is also overlaid.

Supplementary Results

The dynamic evolution of actin domains is independent of threshold actin concentration

To ensure that the domain architecture observed in the actin density fields at 40μM threshold concentration is not limited by choice of threshold concentration, we also studied the actin dynamics at 20μM and 30μM thresholds (Figure S9). We see that while the threshold concentration affects the number of high-density actin domains observed, it does not drastically alter the dynamics of actin domains. Thus, our observations reported in the main text are robust to the choice of F-actin concentration. It is worth noting that extremely high threshold concentrations will result in a different picture of actin organization (Figure 2B) but will be a misleading picture as it will include only a tiny fraction of total actin in the network (Figure 2C).

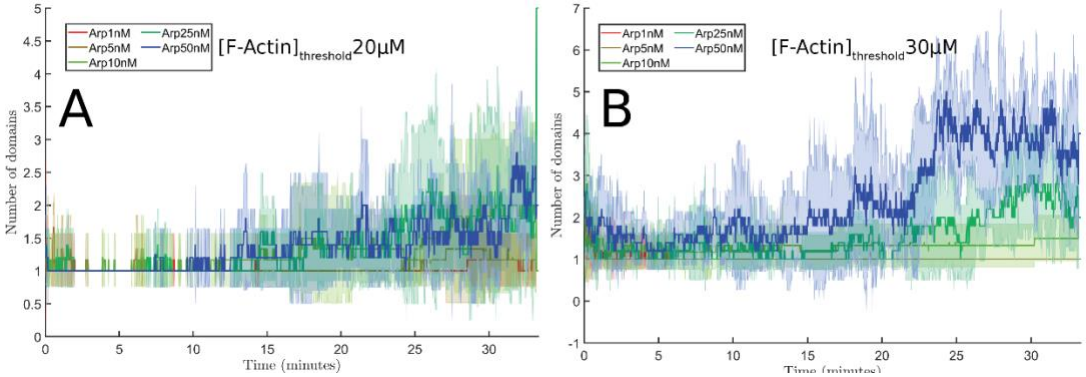

Figure S9. Arp2/3 dependent actin organization is independent of threshold concentration. The time profile of the number of high-density actin domains found by varying Arp2/3 concentration is shown. High-density domains were detected at A. 20 μM and 30 μM local actin concentration thresholds. The solid line and shaded area represent mean and standard deviation, respectively (Sampling frequency=1s).

Supplementary Methods

1. Mechanochemical Dynamics of Active Matter (MEDYAN)

MEDYAN (1) is a C++ based software to simulate mechanochemical dynamics of active matter with special implementations to enable the simulation of filamentous active matter such as actin and microtubules. MEDYAN enables spatially resolved chemical evolution of the reaction network along with physical realism thereby accounting for mechanochemical feedback wherein forces affect reaction chemistry. Here, we outline the key physicochemical paradigms implemented in MEDYAN. In MEDYAN, the filamentous phase and the filament-bound particles are explicitly represented in three-dimensional space while the diffusing pool of molecules are represented as a density field using finite elements.

1.1. Mechanical model of filamentous network

Active filaments are represented as a series of rigid cylinders in three dimensions that resist bending but allow for bending deformations at hinge points. The cylinder length, L_{cyl} (40 monomers, 108nm) is carefully chosen to approximate the curvature of the filaments under contractile forces. Filaments can stretch with stretching constant $K_{fil,str}$ while bending energy, ε_{bend} at hinge points is calculated from the persistence length (L_p) of actin filament as $L_p.k_BT = \varepsilon_{bend}.L_{cyl}$) where k_B represents the Boltzmann constant and temperature T=298K.Additionally, any two cylinders are prevented from overlapping through a cylinder-cylinder excluded volume potential (18). Thus, the mechanical energy of each filament represented by N points in coordinate space is given by the following terms.

$$E_{fil,str} = \sum_{i=1}^{N-1} K_{fil,str}\left(L_{i,i+1} - L_{cyl}\right)^2,$$

$$E_{fil,bend} = \sum_{i=1}^{N-2} \epsilon_{bend} \cos(\pi - \theta_{i,i+1,i+2}).$$

Here, $L_{i,i+1}$ represents the length of cylinder formed by points i and i+1 and $\theta_{i,i+1,i+2}$ represents the angle between points i, i+1, and i+2.

Excluded volume interaction between two cylinder segments is calculated based on the distance r(s,t) between any two points on the cylinder denoted by parameters s and t.

$$E_{fil,vol} = \mathrm{K_{vol}} \int_0^1 \int_0^1 r(s,t)^{-4} ds dt.$$

A more detailed discussion on the excluded volume constant and the physical implication of the functional form can be found here (18).

1.2. Mechanical model of crosslinkers and motor proteins

In MEDYAN, upon a crosslinker/motor binding event, the binding sites are coupled by an elastic spring. This energetic coupling constants for crosslinkers and myosins are given by $K_{\alpha,str}$ and $K_{NMII,str}$ respectively. In this study, motor proteins are represented as NMIIA minifilaments which are small ensembles of non-processive, bipedal proteins. The mechanochemical properties and the stochastic dynamics of minifilaments are represented by the parallel cluster model.(11) Upon minifilament binding, the total number of myosin heads (N_t) is randomly assigned (between 15 and 30 in this study). The stretching constant of the minifilament is assumed to scale linearly with the number of heads as $K_{MF} = K_{NMII,str}.N_t$. Consider two actin filaments that are bound by either a crosslinker or myosin and the binding sites are separated by a distance, L. The mechanical energy due to crosslinker and minifilament coupling are given by,

$$E_{\alpha,str} = K_{\alpha,str}(L - l_0^{\alpha})^2,$$

$$E_{MF,str} = K_{MF,str}(L - l_0^{MF})^2$$

Here, l_0^{α} and l_0^{MF} represent the separation of binding sites at binding.

Mechanical representation of branch points

In MEDYAN, Arp2/3-driven dendritic nucleation leads to the formation of an offspring filament at 70^o with respect to the parent filament. The bound Arp2/3 molecule is represented through a set of interaction potentials that penalize stretching, bending, and dihedral displacements. Figure S10 shows an illustration of the stretching, two bending and one dihedral potentials and the geometric consequences of each.

$$E_{branch,str} = K_{branch,str}(L - L_o)^2,$$

$$E_{branch,bend} = \epsilon_{branch,bend}\cos(\theta - \theta_0),$$

$$E_{branch,dihedral} = \eta_{branch,dihedral}\cos(\overrightarrow{n1},\overrightarrow{n2}).$$

Here, L represents the distance between binding site on the parent filament and the minus-end of the offspring filament (L_o=6nm). For the primary bending potential, θ represents the angle between parent filament and offspring filament ($\theta_0 = 70^o$). For the secondary bending potential, θ represents the angle formed by plus-end of parent cylinder, the binding site on parent cylinder, and the minus end of offspring cylinder ($\theta_0 = 90^o$). $\overrightarrow{n1}$, and $\overrightarrow{n2}$ represent normal of planes as illustrated in Figure S10.

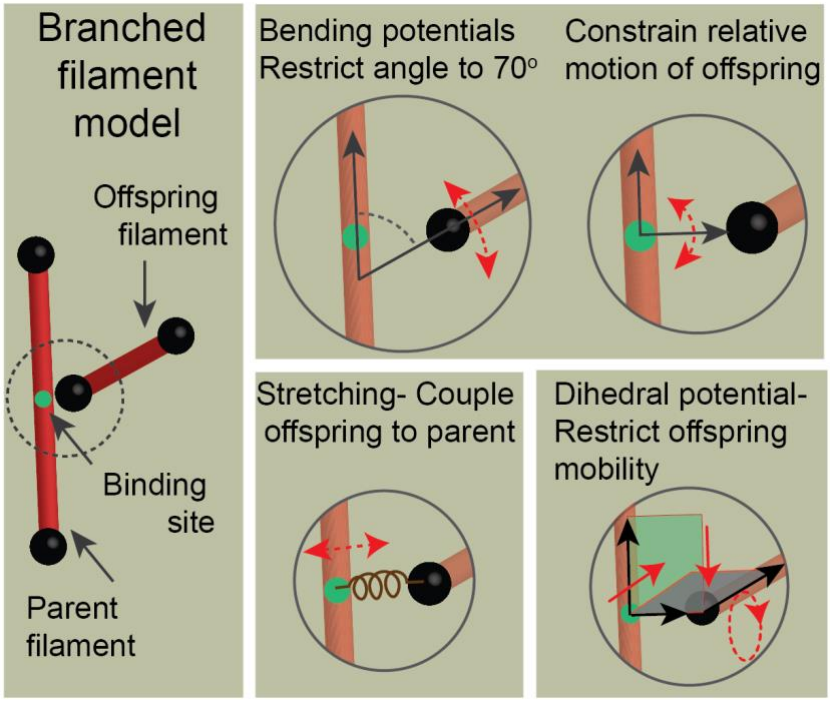

Figure S10. Mechanical energy potentials to represent dendritic branching. Parent and offspring filament segments are shown with cylinder endpoints shown as black spheres. The binding site on the parent filament is shown in green. Panels show various energetic potentials considered and the red dotted arrow represents the corresponding degree of freedom that is restricted.

1.3. Chemical reactions considered

We define the following chemical species in our reaction network.

Chemical species	**Represents**
AD	Diffusing Actin (G-actin)
FA	Filamentous Actin
PE	Plus End
ME	Minus End
MEX	Chemically inactive Minus End
BD	Diffusing brancher
MD	Diffusing myosin minifilament
LD	Diffusing crosslinker
BA	Brancher adhered filamnet end
MA	Filament adhered motor minifilament
LA	Filament adhered linker
FAF	F-actin free of any binding molecule
FAO	F-actin occupied by a binding molecule (M-motor, L-linker)

Table 3: Table of chemical species considered in the rection networks analyzed in this study.
The following chemical reactions have been considered.

$$PE + AD \underset{k^{+}_{actin,depoly}}{\overset{k^{+}_{actin,poly}}{\rightleftharpoons}} FA + PE$$

$$ME + AD \underset{k^{-}_{actin,depoly}}{\overset{k^{-}_{actin,poly}}{\rightleftharpoons}} FA + ME$$

$$BD + AD + FAF \xrightarrow{k_{Arp,bind}} FAO.BA.MEX$$

$$FAO.BA.MEX \xrightarrow{k_{Arp,unbind}} ME + BD + FAF$$

$$MD + 2FAF \underset{k_{MF,unbind}}{\overset{k_{MF,bind}}{\rightleftharpoons}} MA + 2FAOM$$

$$LD + 2FAF \underset{k_{\alpha,unbind}}{\overset{k_{\alpha,bind}}{\rightleftharpoons}} LA + 2FABL$$

$$FAO.M_N + FAF_{N+1} \xrightarrow{k_{MF,walking}} FAF_N + FAO.M_{N+1}$$

Please note that the binding molecule-free F-actin sites should be identified for linker and motor reactions separately such that they are within the respective binding distances ($d_{\alpha,bind}$ and $d_{NMII,bind}$). Additionally, in this study we assume there are four binding sites for actin binding proteins per full length cylinder segment to account for excluded volume interactions between bound molecules.

1.4. Time evolution of reaction network

As seen above, chemical reactions in MEDYAN involve interactions between diffusing molecules and the filamentous phase resulting in a network of reactions that are interdependent on one another. As biological systems often have species at low copy numbers, uniform mixing of all species in the entire reaction volume is physically unreasonable, the reaction volume is divided into sub-volumes (cubes of size 500 nm). The choice of compartment size is guided by the Kuramoto length (19, 20) which represents the reactive mean free length of the fastest reaction in the network (actin plus end polymerization). Further, deterministic techniques have been shown to be inaccurate at low copy numbers and hence it is necessary to consider the stochastic evolution

of such reaction networks. In MEDYAN, we use a computationally optimal version of Gillespie's method (21) called the next reaction method (22). For each reaction, Ri, i [0,N], the execution times τ_μ are randomly calculated based on the propensity ai as $(\tau_\mu = (1/a_\mu) ln (1/r_\mu))$. The reaction with the lowest $\tau_\mu$is executed followed by a dependency update. During the dependency update, all the reactions that share chemical species with Rμ are updated and the corresponding firing rates are recalculated. The series of steps explained above are iteratively repeated to generate the time course of chemical events in a trajectory.

1.5. Mechanochemical considerations

As spatially-resolved Gillespie is essential to capture the mechanochemical realism of cellular active networks, trajectory evolution in MEDYAN involves short bursts of chemical evolution ($\delta_{chemistry}$=25ms in this study) followed by mechanical equilibration to dissipate the stresses accumulated in the system (minimum force in the system F_T=10pN). This separation is based on the underlying assumption that the time scale of chemical evolution is slower than the timescale of mechanical equilibration and that the chemical events do not accumulate excessive stresses that alter the time course of the trajectory.

In addition, experimental evidence suggests that kinetics of specific chemical reactions such as crosslinker/brancher/minifilament unbinding, and minifilament walking are affected by tensions experienced by the chemical species. To account for such variations, we update the chemical rates of such reactions at the end of each minimization cycle using the Bell's formula (23–26) as,

$$k_{\alpha,unbind} = k^0_{\alpha,unbind} \cdot exp\left(\frac{F_{ext}}{F_{\alpha,unbind}}\right),$$

$k_{\alpha,unbind}$ represents the unbinding rate of a crosslinker with a residual tension $F_{ext} = K_{\alpha,str}(L - l_0^{\alpha})$, where L and l_0^{α} represent the current length and equilibrium length of crosslinkers respectively. The zero-force unbinding rate is given by $k_{\alpha,unbind}^0$.

Similarly, the force-sensitive unbinding rate of a brancher is given by,

$$k_{Arp,unbind} = k_{Arp,unbind}^0 \cdot exp\left(\frac{F_{ext}}{F_{B,unbind}}\right),$$

where F_{ext} represents the force on the minus-end of offspring filament resulting from the branching forcefields described above.

The corresponding expression for minifilaments with a total of N_t heads is obtained from parallel cluster model (11). The unbinding rate of minifilament was derived by Erdmann et. al in Ref. (11) and is given by,

$$k_{MF,unbind} = k_{MF,unbind}^0 . \exp\left(-\frac{F_{ext}}{N_b(F_{ext})\mathrm{F_{NMII,unbind}}}\right),$$

where $k_{MF,unbind}^0$ is the zero-force unbinding rate, $F_{ext} = K_{MF,str}(L - l_0^{MF})$, $N_b(F_{ext})$ represents the force-sensitive number of bound heads, and $\mathrm{F_{NMII,unbind}}$ is the characteristic unbinding force per head.

The force-sensitive number of bound heads is given by,

$$N_b(F_{ext}) = \min\left(N_t, \rho N_t + \beta F_{ext}/N_t\right)$$

The zero-force unbinding rate is given by,

$$k_{MF,unbind}^0 \approx \frac{k_{head,bind} N_t}{exp\left(\mathrm{N_t}\log\left(\frac{1}{1-\rho}\right)\right) - 1},$$

where $\rho = k_{head,bind}/(k_{head,bind} + k_{head,unbind})$ represents the duty ratio of individual motors that make the minifilament.

Additionally, the walking rate of motor is also affected by F_{ext} as follows.

$$k_{MF,walk} = k^0_{MF,walk} \frac{\mathrm{F}_{NMII,stall} - \mathrm{F}_{\mathrm{ext}}}{\mathrm{F}_{NMII,stall} + \mathrm{F}_{\mathrm{ext}}/\alpha},$$

given $k^0_{MF,walk}$, the zero-force walking rate, $\mathrm{F}_{NMII,stall}$ the minifilament stall rate, and tunable parameter α. The zero-force walking rate is given by,

$$k^0_{MF,walk} = s k_{head,bind} \frac{1-\rho}{\rho}$$

Here, $s = \mathrm{d}_{\mathrm{step}}\mathrm{N}_{\mathrm{b,sites}}/L_{cyl}$ represents the stepping fraction. This is done to define the walking reaction rate between two binding sites which are separated by $\mathrm{L}_{\mathrm{cyl}}/\mathrm{N}_{\mathrm{b,sites}}$. The tunable parameters α, β, were obtained by fitting the equations to NMII data.

1.6. Force balance for actin-binding proteins

In MEDYAN, the energy minimization step is executed over the points $\{\mathbf{r_i}\}$ that represent the points on the filament. Forces acting on each filament point is given by the gradient, $\mathbf{F}(\mathbf{r_i}) = -\nabla E(\mathbf{r_i})$, where E is the total energy calculated according to the forcefields described above. We employ a variant of the conjugate gradient minimization (27, 28) method known as the Polak–Ribière algorithm (29, 30) to obtain the energy-minimized configuration of the actin network characterized by $|\mathbf{F}(\mathbf{r_i})| \leq \mathrm{F_T}$. During minimization, the forces acting along crosslinkers, and myosins are transformed according to the lever rule to forces that act along the respective filament points. Let us assume that points $\mathbf{r_i}$ and $\mathbf{r_{i+1}}$ along a filament contain a binding site at position $x = |\boldsymbol{r_x} - \boldsymbol{r_i}|/|\boldsymbol{r_i} - \boldsymbol{r_{i+1}}|$ with an actin-binding protein (crosslinker, or myosin). As ABPs are bound two such binding sites, one site experiences a force $F_x = k(l - l_0^{\alpha})$, while the other experiences $-F_x$. As a result, the force F_x is split among filament points as, $F_i = F_x(1-x)$ and $F_{i+1} = F_x.x$.

1.7. Boundary conditions

As the reaction volume is divided into cubic sub-volumes, sub-volumes that are close to the curved surface are partly within and outside the reaction volume. Hence, we make the following modifications to faithfully capture the cylindrical boundary conditions as shown in Figure S11.

1. The diffusion rate between compartments that intersect the boundary surface is scaled by the available interfacial area.
2. The mesoscopic rate constants (c_μ) of reactions are obtained from deterministic rate constants $(k_{\mu)}$ by scaling them based on the volume enclosed within the boundary surface, V_r as follows,

$$c_\mu = k_\mu \left(\frac{V_r}{N_A}\right)^{n-1}$$

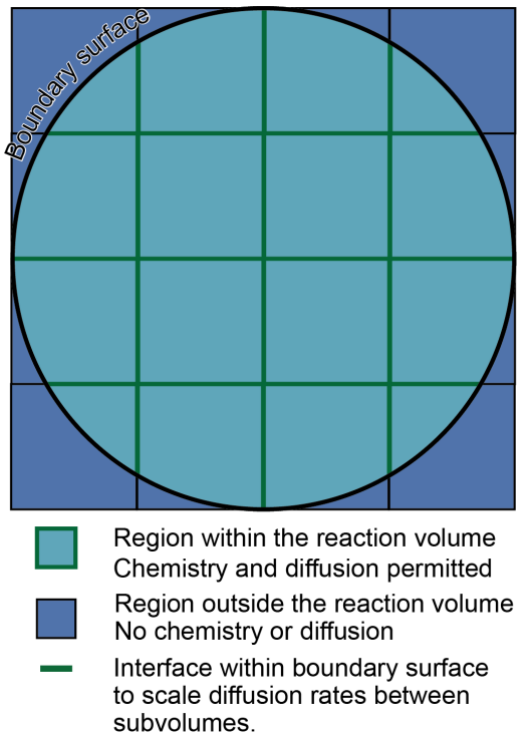

Figure S11. Cartoon of reaction volume cross-section to illustrate chemical boundary conditions. Cartoon shows square sub-volume cross-section along with the boundary surface. Regions outside the reaction volume are shown in dark blue while the regions within the reaction volume are shown in light blue. The interface lengths shown in green are relevant to scale diffusion rates between two compartments.

Diffusion rates of compartments that intersect the boundary layer are scaled in proportion to the interface area enclosed within the sub-volume.

MEDYAN simulations consider enclosed reaction volumes with repulsive boundary conditions. The repulsive energy of the boundary of a filament tip at distance d from the boundary is given by,

$$U_i^{boundary} = \varepsilon_{boundary} e^{-d/\lambda}$$

In addition, Brownian ratchet considerations have also been implemented to ensure that the polymerization rates of free ends reduce as the filament gets closer to the boundary(31).

2. Estimation of drift and diffusion from domain count time-series data

To understand this, we modeled the time series of domain counts from the trajectories at high Arp2/3 concentrations as a stochastic Ito process given by,

$$dN = A(N,t)dt + B(N,t)dW \quad (1)$$

where the number of clusters at time t (N) depends on effective drift term (A) and diffusion coefficient (B). We estimated the effective drift and diffusive terms numerically as,

$$A(n,t) = \lim_{\Delta t \to 0} \frac{\langle N(t+\Delta t) - n \rangle}{\Delta t}\Big|_{N(t)=n} \quad (2)$$

$$B^2(n,t) = \lim_{\Delta t \to 0} \frac{\langle [N(t+\Delta t) - n]^2 \rangle}{\Delta t}\Big|_{N(t)=n} \quad (3)$$

Parameters A and B were estimated at different N(t) values for Δt=1s.

As the above definition of diffusion coefficient still carries the influence of drift(32), we chose to calculate the drift-corrected diffusion coefficient given by,

$$C^2(n,t) = \lim_{\Delta t \to 0} \frac{\langle [N(t+\Delta t) - n - A(n,t)\Delta t]^2 \rangle}{\Delta t}\Big|_{N(t)=n} \quad (4)$$

References

1. Popov, K., J. Komianos, and G.A. Papoian. 2016. MEDYAN : Mechanochemical Simulations of Contraction and Polarity Alignment in Actomyosin Networks. *PLoS Comput. Biol.* 12:e1004877.
2. Fujiwara, I., D. Vavylonis, and T.D. Pollard. 2007. Polymerization kinetics of ADP- and ADP-Pi-actin determined by fluorescence microscopy. *Proc. Natl. Acad. Sci.* 104:8827–8832.
3. Wachsstock, D.H., W.H. Schwartz, and T.D. Pollard. 1993. Affinity of alpha-actinin for actin determines the structure and mechanical properties of actin filament gels. *Biophys. J.* 65:205–14.
4. Kovács, M., F. Wang, A. Hu, Y. Zhang, and J.R. Sellers. 2003. Functional divergence of human cytoplasmic myosin II. Kinetic characterization of the non-muscle IIA isoform. *J. Biol. Chem.* 278:38132–38140.
5. Chandrasekaran, A., A. Clarke, P. Mcqueen, H.Y. Fang, G.A. Papoian, and E. Giniger. 2021. Computational simulations reveal that Abl activity controls cohesiveness of actin networks in growth cones. *bioRxiv doi 10.1101/2021.11.01.466771*. (preprint posted November 2, 2021).
6. Mahaffy, R.E., and T.D. Pollard. 2006. Kinetics of the formation and dissociation of actin filament branches mediated by Arp2/3 complex. *Biophys. J.* 91:3519–3528.
7. Murphy, C.T., R.S. Rock, and J. a Spudich. 2001. A myosin II mutation uncouples ATPase activity from motility and shortens step size. *Nat. Cell Biol.* 3:311–315.
8. Vilfan, A., and T. Duke. 2003. Instabilities in the transient response of muscle. *Biophys. J.* 85:818–827.

9. Billington, N., A. Wang, J. Mao, R.S. Adelstein, and J.R. Sellers. 2013. Characterization of three full-length human nonmuscle myosin II paralogs. *J. Biol. Chem.* 288:33398–33410.

10. Niederman, R., and T.D. Pollard. 1975. Human Platelet Myosin II . In Vitro Assembly and Structure of Myosin Filaments Formation of Platelet Myosin and Myosin Rod Filaments Determination of Platelet Myosin Solubility. *J. Cell Biol.* 67:72–92.

11. Erdmann, T., P.J. Albert, and U.S. Schwarz. 2013. Stochastic dynamics of small ensembles of non-processive molecular motors: The parallel cluster model. *J. Chem. Phys.* 139.

12. Ferrer, J.M., H. Lee, J. Chen, B. Pelz, F. Nakamura, R.D. Kamm, and M.J. Lang. 2008. Measuring molecular rupture forces between single actin filaments and actin-binding proteins. *Proc. Natl. Acad. Sci. U. S. A.* 105:9221–6.

13. Fujiwara, I., S. Suetsugu, S. Uemura, T. Takenawa, and S. Ishiwata. 2002. Visualization and force measurement of branching by Arp2/3 complex and N-WASP in actin filament. *Biochem. Biophys. Res. Commun.* 293:1550–1555.

14. Footer, M.J., J.W.J. Kerssemakers, J.A. Theriot, and M. Dogterom. 2007. Direct measurement of force generation by actin filament polymerization using an optical trap. *Proc. Natl. Acad. Sci.* 104:2181–2186.

15. Didonna, B.A., and A.J. Levine. 2007. Unfolding cross-linkers as rheology regulators in F-actin networks. *Phys. Rev. E - Stat. Nonlinear, Soft Matter Phys.* 75:1–10.

16. Ni, Q., and G.A. Papoian. 2019. Turnover versus Treadmilling in Actin Network Assembly and Remodeling. *Cytoskeleton*. 76:562–570.

17. Mullins, R.D., J.A. Heuser, and T.D. Pollard. 1998. The interaction of Arp2/3 complex

with actin: Nucleation, high affinity pointed end capping, and formation of branching networks of filaments. *Proc. Natl. Acad. Sci.* 95:6181–6186.

18. Floyd, C., A. Chandresekaran, H. Ni, Q. Ni, and G.A. Papoian. 2021. Segmental Lennard-Jones interactions for semi-flexible polymer networks. *Mol. Phys.*

19. Togashi, Y., and K. Kaneko. 2004. Molecular discreteness in reaction-diffusion systems yields steady states not seen in the continuum limit. *Phys. Rev. E - Stat. Physics, Plasmas, Fluids, Relat. Interdiscip. Top.* 70:4.

20. Kuramoto, Y. 1974. Effects of Diffusion on the Fluctuations in Open Chemical Systems. *Progress. Theor. Phys.* 52:711–713.

21. Gillespie, D.T. 1977. Exact stochastic simulation of coupled chemical reactions. *J. Phys. Chem.* 81:2340–2361.

22. Gibson, M.A., and J. Bruck. 2000. Efficient Exact Stochastic Simulation of Chemical Systems with Many Species and Many Channels. *J. Phys. Chem. A.* 104:1876–1889.

23. Bell, G.I. 1978. Models for the Specific Adhesion of Cells to Cells. *Science (80-.).* 200:618–627.

24. Sun, S.X., G. Lan, and E. Atilgan. 2008. Methods in Cell Biology, Chapter 23. Elsevier Inc.

25. Craig, E.M., J. Stricker, M. Gardel, and A. Mogilner. 2015. Model for adhesion clutch explains biphasic relationship between actin flow and traction at the cell leading edge. *Phys. Biol.* 12.

26. Welf, E.S., H.E. Johnson, and J.M. Haugh. 2013. Bidirectional coupling between integrin-mediated signaling and actomyosin mechanics explains matrix-dependent intermittency of leading-edge motility. *Mol. Biol. Cell*. 24:3945–3955.

27. Hager, W.W.W.W., and H. Zhang. 2006. A Survey of Nonlinear Conjugate Gradient Methods. *Pacific J. Optim.* 2:35–58.

28. B. J. Jaidhan, P.S.R.& A.A. 2014. Energy Minimization and Conformation Analysis of Molecules Using Conjugate Gradient Method. *IMPACT Int. J. Res. Eng. Technol. (IMPACT IJRET)*. 2:111–116.

29. Dixon, L.C.W. 1992. Generalized Polak-Ribi re Algorithm. 75:345–354.

30. Touati-Ahmed, D., and C. Storey. 1990. Efficient hybrid conjugate gradient techniques. *J. Optim. Theory Appl.* 64:379–397.

31. Peskin, C.S., G.M. Odell, and G.F. Oster. 1993. Cellular motions and thermal fluctuations: the Brownian ratchet. *Biophys. J.*

32. Devlin, J., D. Husmeier, and J.A. Mackenzie. 2019. Optimal estimation of drift and diffusion coefficients in the presence of static localization error. *Phys. Rev. E*. 100:0–3.